

<sup>1</sup> A novel inf-sup-based volumetric constraint ratio and  
<sup>2</sup> its implementation via mixed FE-meshfree formulation

<sup>3</sup> Junchao Wu<sup>a,\*</sup>, Yingjie Chu<sup>b</sup>, Yangtao Xu<sup>a</sup>

<sup>a</sup> Key Laboratory for Intelligent Infrastructure and Monitoring of Fujian Province, College  
of Civil Engineering, Huaqiao University, Xiamen, Fujian, 361021, China

<sup>b</sup> Fujian Key Laboratory of Digital Simulations for Coastal Civil Engineering, Department  
of Civil Engineering, Xiamen University, Xiamen, Fujian, 361005, China

---

<sup>4</sup> **Abstract**

Numerical formulations for incompressible materials often suffer from volumetric locking, which reduces the accuracy of displacement solutions and introduces oscillations in the pressure field. A well-chosen constraint ratio can mitigate this issue, but traditional approaches lack a theoretical foundation based on the inf-sup (or LBB) condition, which is essential for the stability of mixed formulations. This paper introduces a novel optimal constraint ratio derived from the inf-sup condition to address volumetric locking. The inf-sup test, a numerical tool for verifying the inf-sup condition, is reaffirmed to be equivalent to the inf-sup condition through a variational approach. By incorporating a complete polynomial space whose dimension matches the number of displacement degrees of freedom (DOFs), a new inf-sup value estimator is developed, explicitly considering the constraint ratio. For a given number of displacement DOFs, when the pressure DOFs of a numerical formulation remain below a stabilized number that falls into the optimal constraint ratio range, this numerical formulation actually satisfies the inf-sup condition. To implement the optimal constraint ratio, a mixed finite element and meshfree formulation is proposed, where displacements are discretized using traditional finite element approximations, and pressures are approximated via the reproducing kernel meshfree method. Leveraging the globally smooth reproducing kernel shape functions, the constraint ratio can be flexibly adjusted to meet the inf-sup condition without the limit of element. For computational efficiency and ease of implementation, pressure nodes are placed on selected displacement nodes to maintain the optimal constraint ratio. Inf-sup tests and a series of 2D and 3D incompressible elasticity examples validate the proposed constraint ratio, demonstrating its effectiveness in eliminating volumetric locking and enhancing the performance of mixed finite element and meshfree formulations.

<sup>5</sup> **Keywords:** Optimal constraint ratio, Inf-sup condition estimator, Volumetric  
<sup>6</sup> locking, Mixed formulation, Reproducing kernel meshfree approximation

---

<sup>\*</sup>Corresponding author

Email address: jcwu@hqu.edu.cn (Junchao Wu)  
Preprint submitted to Elsevier

September 8, 2025

7      **1. Introduction**

8      The volumetric constraint is a necessary condition in the numerical formulation  
 9      of incompressible materials like rubber and hydrogel. Proper imposition of  
 10     this constraint is crucial for obtaining better numerical solutions; insufficient or  
 11     excessive constraints will reduce the accuracy and stability of the solution [1].  
 12     The volumetric constraint ratio [2], denoted as  $r$ , is often used to measure the  
 13     level of constraint. It is defined as the total degrees of freedom (DOFs) of dis-  
 14     placement divided by the total DOFs of pressure. Ideally, the optimal constraint  
 15     ratio should be consistent with its governing partial differential equations. For  
 16     example, in the two-dimensional (2D) case, the optimal constraint ratio is 2,  
 17     since there are two governing equations for displacement and one for pressure.  
 18     When the constraint ratio is less than 2, the formulation suffers from volumetric  
 19     locking, while a constraint ratio greater than 2 can cause a coarse solution for  
 20     pressure. These observations have been summarized as follows[2]:

$$r = \frac{2n_u}{n_p}, \quad \begin{cases} r > 2 & \text{too few constraints} \\ r = 2 & \text{optimal} \\ r < 2 & \text{too many constraints} \\ r \leq 1 & \text{severe locking} \end{cases} \quad (1)$$

21     where  $n_u$  and  $n_p$  are the numbers of control nodes for displacement and pressure,  
 22     respectively. Classifying the locked status via the constraint ratio is straight-  
 23     forward but imprecise. For instance, the constraint ratio can remain 2 while  
 24     the pressure is discretized using continuous shape functions identical to the  
 25     displacement's approximation. However, volumetric locking still exists in this  
 26     formulation [2].

27     The inf-sup condition, also known as the Ladyzhenskay–Babuška–Brezzi  
 28     (LBB) condition [3, 4], is a more precise requirement for a locking-free for-  
 29     mulation. This condition is based on the mixed formulation framework, and  
 30     when the inf-sup condition is satisfied, both the accuracy and stability of the  
 31     mixed-formulation can be ensured. However, verifying the inf-sup condition is  
 32     non-trivial. An eigenvalue problem namely inf-sup test can be used to check  
 33     this condition numerically [5, 6, 7, 8]. Analytically, Brezzi and Fortin proposed  
 34     a two-level projection framework that always satisfies the inf-sup condition, al-  
 35     lowing it to be checked by identifying whether the formulation is included in  
 36     this framework. Both analytical and numerical methods to check the inf-sup  
 37     condition are complex, and the relationship between the constraint ratio and  
 38     the inf-sup condition remains unclear.

39     To address volumetric constraint issues, adjusting the constraint ratio to an  
 40     appropriate level is commonly used and easily implemented. In traditional finite  
 41     element methods (FEM), this adjustment is carried out based on elements since  
 42     the DOFs are embedded in each element. Conventional FEM often exhibits  
 43     an over-constrained status. Reducing the approximation order of pressure in  
 44     mixed formulation can alleviate the constraint burden, such as with the well-  
 45     known Q4P1 (4-node quadrilateral displacement element with 1-node piecewise

constant pressure element) and Q8P3. Globally, using continuous shape functions to link the local pressure DOFs in each element can also reduce the total number of pressure DOFs and increase the constraint ratio, such as with T6C3 (6-node triangular displacement element with 3-node continuous linear pressure element) and Q9C4 (Taylor–Hood element) [9]. These schemes belong to the mixed formulation framework and can also be implemented through a projection approach, where the pressure approximant is projected into a lower-dimensional space. Examples include selective integration methods [10, 11], B–bar or F–bar methods [12, 13, 14, 15], pressure projection methods [16, 17, 18, 19, 20], and enhanced strain method [21]. Meanwhile, conventional 3-node triangular elements arranged in a regular cross pattern can also reduce the dimension of the pressure space [22]. It should be noted that not all of these methods meet the inf–sup condition despite alleviating volumetric locking and producing a good displacement solution. Some methods, like Q4P1, show significant oscillation for the pressure solution, known as spurious pressure mode or checkerboard mode [22]. In such cases, additional stabilization approaches, such as variational multi-scale stabilization (VMS) [23, 24, 25, 26, 27], Galerkin/least-squares (GLS) [28], or Streamline upwind/Petrov–Galerkin formulation (SUPG) [29, 30] are required to eliminate the oscillations in pressure.

Another class of FEM methods adjusts the constraint ratio by increasing the displacement DOFs. For instance, based on 3-node triangular elements, Arnold et al. [31, 32] used a cubic bubble function in each element to increase the displacement DOFs, known as the MINI element. It has been shown that this method belongs to the VMS framework [33], and its fulfillment of the inf–sup condition can be analytically evidenced using the two-level projection framework [7]. The Crouzeix–Raviart element [34] transfers the DOFs from the triangular vertices to edges, increasing the constraint ratio since, for triangular topology, the number of edges is greater than that of vertices. More details about FEM technology for volumetric constraint issues can be found in Refs. [2, 4, 35].

In the past two decades, various novel approximations equipped with globally smooth shape functions, such as moving least-squares approximation [36], reproducing kernel approximation [37, 38], radial basis functions [39, 40], maximum-entropy approximation [41], and NURBS approximation [42, 43], have been proposed. In these approaches, the approximant pressure evaluated by the derivatives of globally continuous shape functions also maintains a constraint ratio of 2 in 2D incompressible elasticity problems. However, the corresponding results still show lower accuracy caused by locking [44, 45]. Widely-used locking-free technologies for FEM are introduced in these approaches to enhance their performance. For example, Moutsanidis et al. [46, 47] employed selective integration and B–bar, F–bar methods for reproducing kernel particle methods. Wang et al. [48] applied selective integration schemes with bubble-stabilized functions to node-based smoothed particle FEM. Elguedj et al. [49] proposed the B–bar and F–bar NURBS formulations for linear and nonlinear incompressible elasticity. Chen et al. [50] adopted the pressure projection approach for reproducing kernel formulations for nearly-incompressible problems, which was later extended

to Stokes flow formulations by Goh et al. [51]. Bombarde et al. [52] developed a block-wise NURBS formulation for shell structures, eliminating locking via pressure projection. Casquero and Golestanian [53] proposed a NURBS-based continuous-assumed-strain element to alleviate volumetric locking. Most of these approximations offer better flexibility for arranging DOFs since their shape function constructions are no longer element-dependent. Huerta et al.[54] proposed a reproducing kernel approximation with divergence-free basis functions to avoid volumetric strain entirely , although this approach is unsuitable for compressible cases. Wu et al. [55] added extra displacement DOFs in FEM elements to resolve the locking issue, constructing local shape functions using generalized meshfree interpolation to maintain consistency. Vu-Huu et al. [56] employed different-order polygonal finite element shape functions to approximate displacement and pressure, embedding a bubble function in each element for stabilization.

This work proposes a more precise optimal volumetric constraint ratio and implements a locking-free mixed FE-meshfree formulation with this optimal constraint ratio. Firstly, the inf-sup condition is derived in a new form, showing that the inf-sup value equals to the lowest non-zero eigenvalue of dilatation stiffness in the context of variational analysis. Subsequently, involving a complete polynomial space with dimensions identical to displacement DOFs, the number of non-zero eigenvalues can be analytically calculated, and a new estimator considering the constraint ratio is established. From this estimator, the optimal constraint ratio is defined with a stabilized number of pressure nodes. If the constraint ratio exceeds the locking ratio, the formulation will show severe locking. When the constraint ratio is lower than the optimal ratio, the formulation achieves satisfactory results, and the inf-sup condition is fulfilled. This estimator provides a strong link between the inf-sup value and the pressure DOFs, making it possible to justify the locking status by counting the pressure nodes. Furthermore, a mixed FE-meshfree formulation is proposed to verify the optimal constraint ratio. In this mixed formulation, the displacement is approximated by traditional finite element methods, and the pressure is discretized by reproducing kernel meshfree approximation. With the aid of global RK shape functions, the pressure's DOFs can be adjusted arbitrarily without considering approximation order and numerical integration issues to maintaining the constraint ratio as optimal.

The remainder of this paper is organized as follows: Section 2 reviews the mixed formulation framework for incompressible elasticity problems. In Section 3, a novel estimator of the inf-sup value is developed, from which the optimal constraint ratio is obtained. Section 4 introduces the mixed FE-meshfree formulation and its corresponding nodal distribution schemes. Section 5 verifies the proposed optimal constraint ratio using a set of benchmark incompressible elasticity examples, studying error convergence and stability property for the mixed FE-meshfree approximation. Finally, the conclusions are presented in Section 6.

<sup>136</sup> **2. Mixed-formulation**

<sup>137</sup> *2.1. Nearly-incompressible elasticity*

<sup>138</sup> Consider a body  $\Omega \in \mathbb{R}^{n_d}$  with boundary  $\Gamma$  in  $n_d$ -dimension, where  $\Gamma_t$  and  
<sup>139</sup>  $\Gamma_g$  denote its natural boundary and essential boundary, respectively, such that  
<sup>140</sup>  $\Gamma_t \cup \Gamma_g = \Gamma$ ,  $\Gamma_t \cap \Gamma_g = \emptyset$ . The corresponding governing equations for the mixed  
<sup>141</sup> formulation are given by:

$$\begin{cases} \nabla \cdot \boldsymbol{\sigma} + \mathbf{b} = \mathbf{0} & \text{in } \Omega \\ \frac{p}{\kappa} + \nabla \cdot \mathbf{u} = 0 & \text{in } \Omega \\ \boldsymbol{\sigma} \cdot \mathbf{n} = \mathbf{t} & \text{on } \Gamma_t \\ \mathbf{u} = \mathbf{g} & \text{on } \Gamma_g \end{cases} \quad (2)$$

<sup>142</sup> where  $\mathbf{b}$  denotes the prescribed body force in  $\Omega$ .  $\mathbf{t}, \mathbf{g}$  are prescribed traction and  
<sup>143</sup> displacement on natural and essential boundaries, respectively.  $\mathbf{u}$  and  $p$ , standing  
<sup>144</sup> for displacement and hydrostatic pressure, respectively, are the variables of  
<sup>145</sup> this problem.  $\nabla$  is the gradient tensor defined by  $\nabla = \frac{\partial}{\partial x_i} \mathbf{e}_i$ .  $\boldsymbol{\sigma}$  denotes the  
<sup>146</sup> stress tensor and has the following form:

$$\boldsymbol{\sigma}(\mathbf{u}, p) = p \mathbf{1} + 2\mu \nabla^d \mathbf{u} \quad (3)$$

<sup>147</sup> in which  $\mathbf{1} = \delta_{ij} \mathbf{e}_i \otimes \mathbf{e}_j$  is the second-order identity tensor.  $\nabla^d \mathbf{u}$  is the deviatoric  
<sup>148</sup> gradient of  $\mathbf{u}$  and can be evaluated by:

$$\nabla^d \mathbf{u} = \frac{1}{2} (\mathbf{u} \nabla + \nabla \mathbf{u}) - \left( \frac{1}{3} \nabla \cdot \mathbf{u} \right) \mathbf{1} \quad (4)$$

<sup>149</sup> and  $\kappa, \mu$  are the bulk modulus and shear modulus, respectively, and they can  
<sup>150</sup> be represented by Young's modulus  $E$  and Poisson's ratio  $\nu$ :

$$\kappa = \frac{E}{2(1-2\nu)}, \quad \mu = \frac{E}{3(1+\nu)} \quad (5)$$

<sup>151</sup> In accordance with the Galerkin formulation, the weak form can be given  
<sup>152</sup> by: Find  $\mathbf{u} \in V, p \in Q$ , such that

$$\begin{cases} a(\mathbf{v}, \mathbf{u}) + b(\mathbf{v}, p) = f(\mathbf{v}) & \forall \mathbf{v} \in V \\ b(\mathbf{u}, q) + c(q, p) = 0 & \forall q \in Q \end{cases} \quad (6)$$

<sup>153</sup> with the spaces  $V, Q$  defined by:

$$V = \{\mathbf{v} \in H^1(\Omega)^2 \mid \mathbf{v} = \mathbf{g}, \text{ on } \Gamma_g\} \quad (7)$$

$$Q = \{q \in L^2(\Omega) \mid \int_{\Omega} q d\Omega = 0\} \quad (8)$$

<sup>154</sup> where  $a : V \times V \rightarrow \mathbb{R}$ ,  $b : V \times Q \rightarrow \mathbb{R}$  and  $c : Q \times Q \rightarrow \mathbb{R}$  are bilinear forms,  
<sup>155</sup> and  $f : V \rightarrow \mathbb{R}$  is the linear form. In elasticity problems, they are given by:

$$a(\mathbf{v}, \mathbf{u}) = \int_{\Omega} \nabla^d \mathbf{v} : \nabla^d \mathbf{u} d\Omega \quad (9)$$

$$b(\mathbf{v}, q) = \int_{\Omega} \nabla \cdot \mathbf{v} q d\Omega \quad (10)$$

$$c(q, p) = - \int_{\Omega} \frac{1}{3\kappa} q p d\Omega \quad (11)$$

$$f(\mathbf{v}) = \int_{\Gamma_t} \mathbf{v} \cdot \mathbf{t} d\Gamma + \int_{\Omega} \mathbf{v} \cdot \mathbf{b} d\Omega \quad (12)$$

<sup>156</sup> *2.2. Ritz–Galerkin problem and volumetric locking*

<sup>157</sup> In the mixed-formulation framework, the displacement and pressure can be  
<sup>158</sup> discretized by different approximations. The approximant displacement  $\mathbf{u}_h$  and  
<sup>159</sup> approximant pressure  $p_h$  can be expressed by:

$$\mathbf{u}_h(\mathbf{x}) = \sum_{I=1}^{n_u} N_I(\mathbf{x}) \mathbf{u}_I, \quad p_h(\mathbf{x}) = \sum_{K=1}^{n_p} \Psi_K(\mathbf{x}) p_K \quad (13)$$

<sup>160</sup> where  $N_I$  and  $\Psi_K$  are the shape functions for the displacement and pressure,  $\mathbf{u}_I$   
<sup>161</sup> and  $p_K$  are the corresponding coefficients. Leading these approximations into  
<sup>162</sup> the weak form of Eq. (6) yields the following Ritz–Galerkin problems: Find  
<sup>163</sup>  $\mathbf{u}_h \in V_h$ ,  $p_h \in Q_h$ , such that

$$\begin{cases} a(\mathbf{v}_h, \mathbf{u}_h) + b(\mathbf{v}_h, p_h) = f(\mathbf{v}_h) & \forall \mathbf{v}_h \in V_h \\ b(\mathbf{u}_h, q_h) + c(q_h, p_h) = 0 & \forall q_h \in Q_h \end{cases} \quad (14)$$

<sup>164</sup> where the spaces  $V_h \subseteq V$ ,  $Q_h \subseteq Q$  are defined by:

$$V_h = \{\mathbf{v}_h \in (\text{span}\{N_I\}_{I=1}^{n_u})^{n_d} | \mathbf{v}_h = \mathbf{g}, \text{ on } \Gamma_g\} \quad (15)$$

$$Q_h = \{q_h \in \text{span}\{\Psi_K\}_{K=1}^{n_p} | \int_{\Omega} q_h d\Omega = 0\} \quad (16)$$

<sup>165</sup> For nearly incompressible material, the Poisson ratio approaches 0.5, and  
<sup>166</sup> the bulk modulus  $\kappa$  will tend to infinity based on Eq. (5). Then, the bilinear  
<sup>167</sup> form  $c$  in Eq. (11) tends to zero. And the weak form of Eq. (14) becomes an  
<sup>168</sup> enforcement of the volumetric strain  $\nabla \cdot \mathbf{u}_h$  to be zero using the Lagrangian  
<sup>169</sup> multiplier method, where  $p_h$  is the Lagrangian multiplier.

<sup>170</sup> Furthermore, from the second line of Eq. (14), we have:

$$b(\mathbf{u}_h, q_h) + c(q_h, p_h) = (q_h, \nabla \cdot \mathbf{u}_h) - (q_h, \frac{1}{3\kappa} p_h) = 0, \quad \forall q_h \in Q_h \quad (17)$$

<sup>171</sup> or

$$(q_h, 3\kappa \nabla \cdot \mathbf{u}_h - p_h) = 0, \quad \forall q_h \in Q_h \quad (18)$$

<sup>172</sup> where  $(\bullet, \bullet)$  is the inner product operator evaluated by:

$$(q, p) := \int_{\Omega} q p d\Omega \quad (19)$$

<sup>173</sup> Obviously, in Eq. (18),  $p_h$  is the orthogonal projection of  $3\kappa \nabla \cdot \mathbf{u}_h$  with respect  
<sup>174</sup> to the space  $Q_h$  [1], and, for further development, we use the nabla notation  
<sup>175</sup> with an upper tilde to denote the projection operator, i.e.,  $p_h = \tilde{\nabla} \cdot \mathbf{u}_h$ . In this  
<sup>176</sup> circumstance, the bilinear form  $b$  in the first line of Eq. (14) becomes:

$$\begin{aligned} b(\mathbf{v}_h, p_h) &= (\underbrace{\nabla \cdot \mathbf{v}_h - \tilde{\nabla} \cdot \mathbf{v}_h, p_h}_{0}) + (\tilde{\nabla} \cdot \mathbf{v}_h, \underbrace{p_h}_{3\kappa \tilde{\nabla} \cdot \mathbf{u}_h}) \\ &= (\tilde{\nabla} \cdot \mathbf{v}_h, 3\kappa \tilde{\nabla} \cdot \mathbf{u}_h) \\ &= \tilde{a}(\mathbf{v}_h, \mathbf{u}_h) \end{aligned} \quad (20)$$

<sup>177</sup> where the bilinear form  $\tilde{a} : V_h \times V_h \rightarrow \mathbb{R}$  is defined by:

$$\tilde{a}(\mathbf{v}_h, \mathbf{u}_h) = \int_{\Omega} 3\kappa \tilde{\nabla} \cdot \mathbf{v}_h \tilde{\nabla} \cdot \mathbf{u}_h d\Omega \quad (21)$$

<sup>178</sup> Accordingly, the problem of Eq. (14) becomes a one-variable form: Find  
<sup>179</sup>  $\mathbf{u}_h \in V_h$ , such that

$$a(\mathbf{v}_h, \mathbf{u}_h) + \tilde{a}(\mathbf{v}_h, \mathbf{u}_h) = f(\mathbf{v}_h), \quad \forall \mathbf{v}_h \in V_h \quad (22)$$

<sup>180</sup> As  $\kappa \rightarrow \infty$ , Eq. (22) can be regarded as an enforcement of volumetric strain  
<sup>181</sup> using the penalty method, where  $\tilde{a}$  is the penalty term. However, it should  
<sup>182</sup> be noted that, if the mixed-formulation wants to obtain a satisfactory result,  
<sup>183</sup> this orthogonal projection must be surjective [57]. In the case where it is not  
<sup>184</sup> surjective, for a given  $p_h \in Q_h$ , it may not be possible to find a  $\mathbf{u}_h \in V_h$  such that  
<sup>185</sup>  $p_h = 3\kappa \nabla \cdot \mathbf{u}_h$ . This will lead to a much smaller displacement than expected and  
<sup>186</sup> an oscillated pressure result. This phenomenon is called volumetric locking.

### <sup>187</sup> 3. Optimal volumetric constraint ratio

#### <sup>188</sup> 3.1. Inf-sup condition and its eigenvalue problem

<sup>189</sup> To ensure the surjectivity of orthogonal projection and satisfactory results,  
<sup>190</sup> the approximations of Eq.(7) should satisfy the inf-sup condition, also known  
<sup>191</sup> as the Ladyzhenskaya-Babuška-Brezzi condition [4]:

$$\inf_{q_h \in Q_h} \sup_{\mathbf{v}_h \in V_h} \frac{|b(q_h, \mathbf{v}_h)|}{\|q_h\|_Q \|\mathbf{v}_h\|_V} \geq \beta > 0 \quad (23)$$

<sup>192</sup> in which  $\beta$ , namely the inf-sup value, is a constant independent of the char-  
<sup>193</sup> acterized element size  $h$ . The norms  $\|\bullet\|_V$  and  $\|\bullet\|_Q$  can be flexibly defined

<sup>194</sup> by:

$$\|\mathbf{v}\|_V^2 := \int_{\Omega} \nabla^d \mathbf{v} : \nabla^d \mathbf{v} d\Omega \quad (24)$$

$$\|q\|_Q^2 := \int_{\Omega} \frac{1}{3\kappa} q^2 d\Omega \quad (25)$$

<sup>195</sup> Additionally, the Appendix A lists the displacement and pressure error estimators for the mixed-formulations. This indicates how the inf-sup value  $\beta$  affects <sup>196</sup> the solution accuracy.

<sup>198</sup> To establish the relationship between the inf-sup condition and the constraint ratio, the inf-sup condition is firstly transformed by the following Lemma <sup>199</sup> 1:

<sup>201</sup> **Lemma 1.** Suppose  $\mathcal{P}_h : V_h \rightarrow Q_h$  is the orthogonal projection operator of the <sup>202</sup> divergence operator  $\mathcal{P} := 3\kappa \nabla \cdot$ , i.e.,  $\mathcal{P}_h := 3\kappa \tilde{\nabla} \cdot$  and satisfies Eq. (18). Then, <sup>203</sup> the inf-sup value can be estimated by:

$$\beta \leq \inf_{V'_h \subset V_h \setminus \ker \mathcal{P}_h} \sup_{\mathbf{v}_h \in V'_h} \frac{\|\mathcal{P}_h \mathbf{v}_h\|_Q}{\|\mathbf{v}_h\|_V} \quad (26)$$

<sup>204</sup> in which  $\ker \mathcal{P}_h \subset V_h$  is the kernel of  $\mathcal{P}_h$  defined by  $\ker \mathcal{P}_h := \{\mathbf{v}_h \in V_h \mid \mathcal{P}_h \mathbf{v}_h = 0\}$ .

<sup>206</sup> PROOF. First, define the image space of  $\mathcal{P}_h$  as  $\text{Im} \mathcal{P}_h := \{p_h \in Q_h \mid \exists \mathbf{v}_h \in V_h, p_h = \mathcal{P}_h \mathbf{v}_h\}$ . Since  $\mathcal{P}_h \subset Q_h$ , Eq. (23) can be rewritten as:

$$\begin{aligned} \beta &\leq \inf_{q_h \in Q_h} \sup_{\mathbf{v}_h \in V_h} \frac{|b(q_h, \mathbf{v}_h)|}{\|q_h\|_Q \|\mathbf{v}_h\|_V} = \inf_{q_h \in Q_h} \sup_{\mathbf{v}_h \in V_h} \frac{|(q_h, \frac{1}{3\kappa} \mathcal{P} \mathbf{v}_h)|}{\|q_h\|_Q \|\mathbf{v}_h\|_V} \\ &\leq \inf_{q_h \in \text{Im} \mathcal{P}_h} \sup_{\mathbf{v}_h \in V_h} \frac{|\frac{1}{3\kappa} (q_h, \mathcal{P}_h \mathbf{v}_h)|}{\|q_h\|_Q \|\mathbf{v}_h\|_V} \end{aligned} \quad (27)$$

<sup>208</sup> For a given  $q_h \in \text{Im} \mathcal{P}_h$ , since both  $q_h$  and  $\mathcal{P}_h \mathbf{v}_h$  belong to  $\text{Im} \mathcal{P}_h$ ,  $\text{Im} \mathcal{P}_h \subset Q_h$ , <sup>209</sup> according to the Cauchy-Schwarz inequality, we have:

$$\left| \frac{1}{3\kappa} (q_h, \mathcal{P}_h \mathbf{v}_h) \right| \leq \|q_h\|_Q \|\mathcal{P}_h \mathbf{v}_h\|_Q \quad (28)$$

<sup>210</sup> where this equality holds if and only if  $q_h = \mathcal{P}_h \mathbf{v}_h$ , i.e.,

$$\left| \frac{1}{3\kappa} (q_h, \mathcal{P}_h \mathbf{v}_h) \right| = \|q_h\|_Q \|\mathcal{P}_h \mathbf{v}_h\|_Q, \quad \forall \mathbf{v}_h \in V'_h \quad (29)$$

<sup>211</sup> the space  $V'_h \subseteq V_h \setminus \ker \mathcal{P}_h$  defined by:

$$V'_h = \{\mathbf{v}_h \in V_h \mid \mathcal{P}_h \mathbf{v}_h = q_h\} \quad (30)$$

<sup>212</sup> And the following relationship can be evidenced:

$$\sup_{\mathbf{v}_h \in V_h} \frac{|\frac{1}{3\kappa} (q_h, \mathcal{P}_h \mathbf{v}_h)|}{\|q_h\|_Q \|\mathbf{v}_h\|_V} = \sup_{\mathbf{v}_h \in V'_h} \frac{\|\mathcal{P}_h \mathbf{v}_h\|_Q}{\|\mathbf{v}_h\|_V}, \quad \exists q_h \in \text{Im} \mathcal{P}_h \quad (31)$$

<sup>213</sup> Consequently, by combining Eqs. (27) and (31), Eq. (26) can be obtained.

<sup>214</sup> **Remark 1.** With Lemma 1 and the norm definitions in Eqs. (24),(25), the  
<sup>215</sup> square of the inf-sup value can further be bounded by:

$$\beta^2 \leq \inf_{V'_h \subset V_h \setminus \ker \mathcal{P}_h} \sup_{\mathbf{v}_h \in V'_h} \frac{\|\mathcal{P}_h \mathbf{v}_h\|_Q^2}{\|\mathbf{v}_h\|_V^2} = \inf_{V'_h \subset V_h \setminus \ker \mathcal{P}_h} \sup_{\mathbf{v}_h \in V'_h} \frac{\tilde{a}(\mathbf{v}_h, \mathbf{v}_h)}{a(\mathbf{v}_h, \mathbf{v}_h)} \quad (32)$$

<sup>216</sup> The left-hand side of the above equation is consistent with the minimum-maximum  
<sup>217</sup> principle [58] and again proves the equivalence with the traditional numerical  
<sup>218</sup> inf-sup test [5]. Since that,  $\beta^2$  evaluates the non-zero general eigenvalue of  $\tilde{a}$   
<sup>219</sup> and  $a$  in Eq. (22).

### <sup>220</sup> 3.2. Inf-sup value estimator

<sup>221</sup> Subsequently, the relationship between constraint ratio and the inf-sup con-  
<sup>222</sup> dition is established by the following Theorem:

<sup>223</sup> **Theorem 1.** Suppose that  $P_{n_u}$  is a complete polynomial space with  $n_u$  dimen-  
<sup>224</sup> sions, and  $V_{n_u}$  is the polynomial displacement space,  $V_{n_u} = P_{n_u}^{n_d}$ . The inf-sup  
<sup>225</sup> value  $\beta$  can further be bounded by:

$$\beta \leq \beta_s + O(h) \quad (33)$$

<sup>226</sup> with

$$\beta_s = \inf_{V' \subset V_{n_u} \setminus \ker \mathcal{P}_h \mathcal{I}_h} \sup_{\mathbf{v} \in V'} \frac{\|\mathcal{P} \mathbf{v}\|_Q}{\|\mathbf{v}\|_V} \quad (34)$$

<sup>227</sup> where  $\mathcal{I}_h$  is the interpolation operator of the displacement approximation, and  
<sup>228</sup> correspondingly,  $O(h)$  is the remainder related to  $h$ .

<sup>229</sup> PROOF. As the dimensions of  $V_h$  and  $V_{n_u}$  are identical,  $\dim V_{n_u} = \dim V_h =$   
<sup>230</sup>  $n_d \times n_u$ . There exists a unique  $\mathbf{v} \in V_{n_u}$  satisfying  $\mathbf{v}_h = \mathcal{I}_h \mathbf{v}$ . And the right side  
<sup>231</sup> of Eq. (26) becomes:

$$\inf_{V'_h \subset V_h \setminus \ker \mathcal{P}_h} \sup_{\mathbf{v}_h \in V'_h} \frac{\|\mathcal{P}_h \mathbf{v}_h\|_Q}{\|\mathbf{v}_h\|_V} = \inf_{V' \subset V_{n_u} \setminus \ker \mathcal{P}_h \mathcal{I}_h} \sup_{\mathbf{v} \in V'} \frac{\|\mathcal{P}_h \mathcal{I}_h \mathbf{v}\|_Q}{\|\mathcal{I}_h \mathbf{v}\|_V} \quad (35)$$

<sup>232</sup> According to the triangular inequality, Cauchy-Schwarz inequality, and the  
<sup>233</sup> relationship of Eqs. (18), we have:

$$\begin{aligned} \|\mathcal{P}_h \mathcal{I}_h \mathbf{v}\|_Q &= \sup_{q_h \in Q_h} \frac{|\frac{1}{3\kappa}(q_h, \mathcal{P}_h \mathcal{I}_h \mathbf{v})|}{\|q_h\|_Q} = \sup_{q_h \in Q_h} \frac{|\frac{1}{3\kappa}(q_h, \mathcal{P} \mathcal{I}_h \mathbf{v})|}{\|q_h\|_Q} \\ &\leq \sup_{q_h \in Q_h} \frac{|\frac{1}{3\kappa}(q_h, \mathcal{P} \mathbf{v})| + |\frac{1}{3\kappa}(q_h, \mathcal{P} \mathbf{v} - \mathcal{P} \mathcal{I}_h \mathbf{v})|}{\|q_h\|_Q} \\ &\leq \|\mathcal{P} \mathbf{v}\|_Q + \|\mathcal{P}(\mathbf{v} - \mathcal{I}_h \mathbf{v})\|_Q \end{aligned} \quad (36)$$

<sup>234</sup> Obviously, the second term on the right side of Eq. (36) is the interpolation  
<sup>235</sup> error, and can be evaluated by [59]:

$$\|\mathcal{P}(\mathbf{v} - \mathcal{I}_h \mathbf{v})\|_Q \leq Ch^k |\mathbf{v}|_{H_k} \quad (37)$$

236 where, for a sufficiently smooth  $\mathbf{v} \in V$ ,  $k$  equals to the interpolation order of  
 237  $\mathcal{I}_h$ .

238 Further leading the relation  $\|\mathcal{I}_h \mathbf{v}\|_V \geq C|\mathbf{v}|_{H_k}$  obtained from the closed  
 239 graph theorem [33] and considering Eqs. (36)-(37), the right-hand side of Eq.  
 240 (35) can be represented as:

$$\inf_{V' \subset V_{n_u} \setminus \ker \mathcal{P}_h \mathcal{I}_h} \sup_{\mathbf{v} \in V'} \frac{\|\mathcal{P}_h \mathcal{I}_h \mathbf{v}\|_Q}{\|\mathcal{I}_h \mathbf{v}\|_V} \leq \inf_{V' \subset V_{n_u} \setminus \ker \mathcal{P}_h \mathcal{I}_h} \sup_{\mathbf{v} \in V'} \frac{\|\mathcal{P} \mathbf{v}\|_Q}{\|\mathbf{v}\|_V} + O(h) \quad (38)$$

241 Substituting Eqs. (35),(38) into (26) finally proves Eqs. (33), (34).

242 As we can see in Eqs. (33) and (34),  $\beta_s \geq 0$ , the condition that  $\beta_s$  being  
 243 equal to 0 or not determines whether the formulation can satisfy the inf-sup  
 244 condition. If  $\beta_s > 0$ , as the mesh refines, the second term on the right-hand  
 245 side of Eq. (33) will sharply reduce and can be ignored. In contrast, if  $\beta_s = 0$ ,  
 246 the second term will dominate, and the evaluation of  $\beta$  will be dependent to  $h$ .  
 247 Therefore, the inf-sup condition is violated and numerical instability arises.

### 248 3.3. Polynomial-wise constraint counting

249 From the above subsection, we can know that whether  $\beta_s$  is zero or not  
 250 determines whether the mixed-formulation can fulfill the inf-sup condition. Ac-  
 251 cording to the expression of  $\beta_s$  in Eq. (34), as  $\beta_s = 0$ , the variable  $\mathbf{v}$  should  
 252 belong to  $\ker \mathcal{P}$ , so the dimensions of the subspace in which  $\beta_s \neq 0$ , namely  $n_s$ ,  
 253 can be evaluated by:

$$n_s = \dim(V_{n_u} \setminus \ker \mathcal{P}) \quad (39)$$

254 To further construct the relationship between the inf-sup value estimator in  
 255 Eq. (33) and the constraint ratio  $r = \frac{n_d \times n_u}{n_p}$ , we should find the displacement  
 256 and pressure DOFs in Eq. (33). With the definition of  $V_{n_u}$ , the number of  
 257 displacement DOFs is easy to be evaluated by:

$$n_d \times n_u = \dim V_{n_u} \quad (40)$$

258 With well-posed nodal distributions of displacement and pressure, the number  
 259 of pressure DOFs has the following relationship:

$$n_p = \dim Q_h = \dim(\text{Im} \mathcal{P}_h) = \dim(V_{n_u} \setminus \ker \mathcal{P}_h \mathcal{I}_h) \quad (41)$$

260 Figure 1 illustrates how the relationship between  $n_s$ ,  $n_p$ , and  $n_u$  influences  
 261 the fulfillment of the inf-sup condition:

- 262 • As  $n_p > n_s$ , there must exist a subspace in space  $V_{n_u} \setminus \ker \mathcal{P}_h \mathcal{I}_h$  belonging  
 263 to  $\ker \mathcal{P}$ , resulting in  $\beta_s = 0$ , i.e.,  $V_{n_u} \setminus \ker \mathcal{P}_h \mathcal{I}_h \cap \ker \mathcal{P} \neq \emptyset$ . At this cir-  
 264 cumstance, the inf-sup condition cannot be satisfied, and the formulation  
 265 will suffer from volumetric locking.
- 266 • As  $n_p \leq n_s$ , for well-posed nodal distributions, the space  $V_{n_u} \setminus \ker \mathcal{P}_h \mathcal{I}_h$   
 267 may be a subset of  $V_{n_u} \setminus \ker \mathcal{P}$ . Then,  $\beta_s$  will remain nonzero, and the  
 268 formulation will be locking-free.

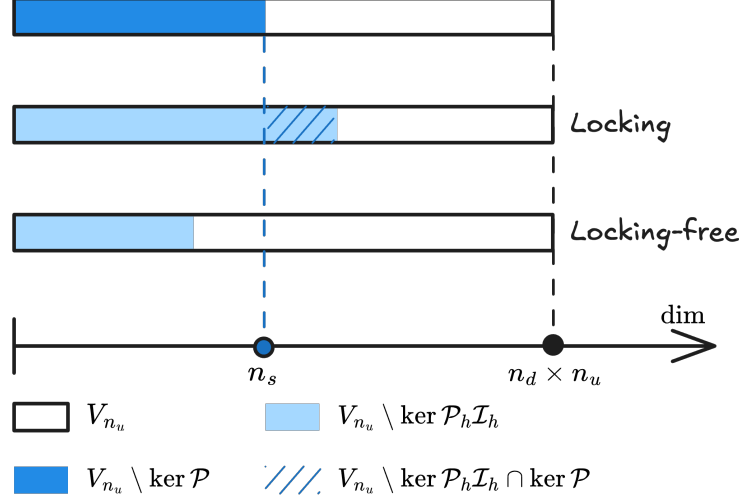


Figure 1: Illustration of estimator

269     Summarily, the formulation can satisfy the inf-sup condition and alleviate  
 270     volumetric locking if at least the number of pressure nodes  $n_p$  is less than  $n_s$ ,  
 271     so we name  $n_s$  as the stabilized number of pressure nodes. At this moment,  
 272     the volumetric constraint ratio should meet the following relation to ensure the  
 273     inf-sup condition:

$$r_{opt} \geq \frac{n_d \times n_u}{n_s} \quad (42)$$

274     **Remark 2.** *Some uniform elements with special arrangements, like the union-*  
 275     *jack element arrangement for 3-node triangular elements, can pass the inf-sup*  
 276     *test [6], but their pressure DOFs number is greater than  $n_s$ . This is because the*  
 277     *union-jack arrangement leads to a lower nonzero eigenvalue number of  $\tilde{\alpha}$  and a*  
 278     *in Eq. (22), and the corresponding nonzero eigenvalue number is less than or*  
 279     *equal to the stabilized number  $n_s$ , satisfying Eq. (42). The similar cases about*  
 280     *this special element arrangement are too few, so it is more straightforward to*  
 281     *use the number of pressure nodes  $n_p$  to measure  $\dim(V_{n_u} \setminus \ker \mathcal{P}_h \mathcal{I}_h)$ .*

282     **Remark 3.** *It is obvious that the traditional optimal constraint ratio cannot*  
 283     *fulfill this condition. However, not all formulations satisfying this condition*  
 284     *can totally avoid volumetric locking. This is because  $n_p \leq n_s$  is not equivalent*  
 285     *to  $V_{n_u} \setminus \ker \mathcal{P}_h \mathcal{I}_h \subset V_{n_u} \setminus \ker \mathcal{P}$ . Fortunately, well-posed nodal distributions of*  
 286     *displacement and pressure can ensure this, which will be evidenced by numerical*  
 287     *examples in the subsequent sections.*

### 288     3.4. Optimal volumetric constraint ratio

289     The fulfillment of the inf-sup condition should require the number of pres-  
 290     sure nodes  $n_p$  to be lower than the stabilized number  $n_s$ , and now, we will  
 291     demonstrate how to determine  $n_s$  for a specific number of displacement DOFs.

<sup>292</sup> In the 2D case, for instance, we first consider the linear polynomial displacement  
<sup>293</sup> space  $V_3$  that is given by:

$$V_3 = \text{span} \left\{ \begin{pmatrix} 1 \\ 0 \end{pmatrix}, \begin{pmatrix} 0 \\ 1 \end{pmatrix}, \begin{pmatrix} x \\ 0 \end{pmatrix}, \begin{pmatrix} 0 \\ x \end{pmatrix}, \begin{pmatrix} y \\ 0 \end{pmatrix}, \begin{pmatrix} 0 \\ y \end{pmatrix} \right\} \quad (43)$$

<sup>294</sup> or rearranged as follows,

$$V_3 = \text{span} \left\{ \underbrace{\begin{pmatrix} 1 \\ 0 \end{pmatrix}, \begin{pmatrix} 0 \\ 1 \end{pmatrix}, \begin{pmatrix} y \\ 0 \end{pmatrix}, \begin{pmatrix} 0 \\ x \end{pmatrix}, \begin{pmatrix} x \\ -y \end{pmatrix}}_{\ker \mathcal{P}}, \underbrace{\begin{pmatrix} x \\ y \end{pmatrix}}_{V_3 \setminus \ker \mathcal{P}} \right\} \quad (44)$$

<sup>295</sup> It can be counted that, for  $n_u = 3$ ,  $n_s = 1$ . Following the path, the displacement  
<sup>296</sup> space with a quadratic polynomial base, namely  $V_6$ , can be stated as:

$$V_6 = \text{span} \left\{ \underbrace{\begin{pmatrix} 1 \\ 0 \end{pmatrix}, \begin{pmatrix} 0 \\ 1 \end{pmatrix}, \begin{pmatrix} y \\ 0 \end{pmatrix}, \begin{pmatrix} 0 \\ x \end{pmatrix}, \begin{pmatrix} x \\ -y \end{pmatrix}, \begin{pmatrix} x^2 \\ -2xy \end{pmatrix}, \begin{pmatrix} y^2 \\ 0 \end{pmatrix}, \begin{pmatrix} 0 \\ x^2 \end{pmatrix}, \begin{pmatrix} -2xy \\ y^2 \end{pmatrix}}_{\ker \mathcal{P}}, \underbrace{\begin{pmatrix} x \\ y \end{pmatrix}, \begin{pmatrix} x^2 \\ 2xy \end{pmatrix}, \begin{pmatrix} 2xy \\ y^2 \end{pmatrix}}_{V_6 \setminus \ker \mathcal{P}} \right\} \quad (45)$$

<sup>297</sup> In this circumstance,  $n_s = 3$ . As the order of the polynomial space increases, the  
<sup>298</sup> optimal numbers of constraint DOFs for each order of the polynomial space are  
<sup>299</sup> listed in Table. 1, in which  $n$  denotes the order of space  $P_{n_u}$ . For the flexibility  
<sup>300</sup> of usage, the relation between  $n_u$  and  $n_s$  is summarized as follows:

$$n_s = \frac{n(n+1)}{2}, \quad n = \left\lfloor \frac{\sqrt{1+8n_u}-3}{2} \right\rfloor \quad (46)$$

<sup>301</sup> where  $\lfloor \bullet \rfloor$  denotes the floor function.

Table 1: Relationship between the number of displacement nodes  $n_u$  and stabilized number of pressure nodes  $n_s$

$n$	2D		3D	
	$n_u$	$n_s$	$n_u$	$n_s$
1	3	1	4	1
2	6	3	10	4
3	10	6	20	10
4	15	10	35	20
$\vdots$	$\vdots$	$\vdots$	$\vdots$	$\vdots$

<sup>302</sup> For the 3D case, following the path in 2D, the linear polynomial space  $V_4$  is

<sup>303</sup> considered herein, and the arranged space of  $V_4$  is listed as follows:

$$V_4 = \text{span} \left\{ \underbrace{\begin{pmatrix} 1 \\ 0 \\ 0 \\ 0 \end{pmatrix}, \begin{pmatrix} 0 \\ 1 \\ 0 \\ 0 \end{pmatrix}, \begin{pmatrix} 0 \\ 0 \\ 1 \\ 0 \end{pmatrix}, \begin{pmatrix} 0 \\ x \\ 0 \\ 0 \end{pmatrix}, \begin{pmatrix} 0 \\ 0 \\ x \\ 0 \end{pmatrix}, \begin{pmatrix} 0 \\ 0 \\ 0 \\ y \end{pmatrix}}_{\ker \mathcal{P}}, \underbrace{\begin{pmatrix} 0 \\ 0 \\ y \\ 0 \end{pmatrix}, \begin{pmatrix} z \\ 0 \\ 0 \\ 0 \end{pmatrix}, \begin{pmatrix} 0 \\ z \\ 0 \\ 0 \end{pmatrix}, \begin{pmatrix} x \\ -y \\ 0 \\ 0 \end{pmatrix}, \begin{pmatrix} x \\ 0 \\ -z \\ 0 \end{pmatrix}, \begin{pmatrix} x \\ y \\ z \\ 0 \end{pmatrix}}_{\ker \mathcal{P}} \right\}_{V_{n_u} \setminus \ker \mathcal{P}} \quad (47)$$

<sup>304</sup> For brevity, the stabilized numbers for higher-order polynomial displacement  
<sup>305</sup> spaces are directly listed in Table. 1, and it can be summarized that, for a given  
<sup>306</sup> number of displacement DOFs, the stabilized number for pressure DOFs can be  
<sup>307</sup> calculated as follows:

$$n_s = \frac{n(n+1)(n+2)}{6} \quad (48)$$

$$n = \left\lfloor \left( 3n_u + \frac{1}{3} \sqrt{81n_u^2 - \frac{1}{3}} \right)^{\frac{1}{3}} + \frac{1}{3 \left( 3n_u + \frac{1}{3} \sqrt{81n_u^2 - \frac{1}{3}} \right)^{\frac{1}{3}}} - 2 \right\rfloor \quad (49)$$

#### <sup>308</sup> 4. Mixed FE–meshfree formulation with optimal constraint ratio

<sup>309</sup> In the proposed mixed–formulation, the displacement is approximated using  
<sup>310</sup> 3-node (Tri3), 6-node (Tri6) triangular elements and 4-node (Quad4), 8-node  
<sup>311</sup> (Quad8) quadrilateral elements in 2D, 4-node (Tet4) tetrahedral element and  
<sup>312</sup> 8-node (Hex8) hexahedral element in 3D [2]. In order to flexibly adjust to let  
<sup>313</sup> the DOFs of pressure meet the optimal constraint, the reproducing kernel (RK)  
<sup>314</sup> meshfree approximation is involved to approximate pressure, namely “FE”–RK  
<sup>315</sup> formulation.

##### <sup>316</sup> 4.1. Reproducing kernel meshfree approximation

<sup>317</sup> In accordance with the reproducing kernel approximation, the entire domain  
<sup>318</sup>  $\Omega$ , as shown in Figure 2, is discretized by  $n_p$  meshfree nodes,  $\{\mathbf{x}_I\}_{I=1}^{n_p}$ . The  
<sup>319</sup> approximated pressure, namely  $p_h$ , can be expressed by the shape function  $\Psi_I$   
<sup>320</sup> and nodal coefficient  $p_I$ , yields:

$$p_h(\mathbf{x}) = \sum_{I=1}^{n_p} \Psi_I(\mathbf{x}) p_I \quad (50)$$

<sup>321</sup> where, in the reproducing kernel approximation framework, the shape function  
<sup>322</sup>  $\Psi_I$  is given by:

$$\Psi_I(\mathbf{x}) = \mathbf{c}(\mathbf{x}_I - \mathbf{x}) \mathbf{p}(\mathbf{x}_I - \mathbf{x}) \phi(\mathbf{x}_I - \mathbf{x}) \quad (51)$$

<sup>323</sup> in which  $\mathbf{p}$  is the basis vector, for instance in the context of the 3D quadratic  
<sup>324</sup> case, the basis vector takes the following form:

$$\mathbf{p}(\mathbf{x}) = \{1, x, y, z, x^2, y^2, z^2, xy, xz, yz\}^T \quad (52)$$

<sup>325</sup> and  $\phi$  stands for the kernel function. In this work, the traditional Cubic B-spline  
<sup>326</sup> function with square or cube support is used as the kernel function:

$$\phi(\mathbf{x}_I - \mathbf{x}) = \phi(s_x)\phi(s_y)\phi(s_z), \quad s_i = \frac{\|\mathbf{x}_I - \mathbf{x}\|}{\bar{s}_{iI}} \quad (53)$$

<sup>327</sup> with

$$\phi(s) = \frac{1}{3!} \begin{cases} (2-2s)^3 - 4(1-2s)^3 & s \leq \frac{1}{2} \\ (2-2s)^3 & \frac{1}{2} < s < 1 \\ 0 & s > 1 \end{cases} \quad (54)$$

<sup>328</sup> where  $\bar{s}_{iI}$ 's are the support size towards the  $i$ -direction for the shape function  
<sup>329</sup>  $\Psi_I$ . The correction function  $\mathbf{c}$  can be determined by the following so-called  
<sup>330</sup> consistency condition:

$$\sum_{I=1}^{n_p} \Psi_I(\mathbf{x}) \mathbf{p}(\mathbf{x}_I) = \mathbf{p}(\mathbf{x}) \quad (55)$$

<sup>331</sup> or equivalent shifted form:

$$\sum_{I=1}^{n_p} \Psi_I(\mathbf{x}) \mathbf{p}(\mathbf{x}_I - \mathbf{x}) = \mathbf{p}(\mathbf{0}) \quad (56)$$

<sup>332</sup> The consistency condition ensures that the reproducing kernel shape functions  
<sup>333</sup> are able to reproduce the polynomial space spanned by the basis function  $\mathbf{p}$ ,  
<sup>334</sup> which is a fundamental requirement for the accuracy of the Galerkin method.  
<sup>335</sup> Herein, the order of the basis function  $\mathbf{p}$  is chosen to be the same as the order  
<sup>336</sup> of the displacement approximation.

<sup>337</sup> Further, substituting Eq. 51 into Eq. (56) leads to:

$$\mathbf{c}(\mathbf{x}_I - \mathbf{x}) = \mathbf{A}^{-1}(\mathbf{x}_I - \mathbf{x}) \mathbf{p}(\mathbf{0}) \quad (57)$$

<sup>338</sup> in which  $\mathbf{A}$  is namely the moment matrix evaluated by:

$$\mathbf{A}(\mathbf{x}_I - \mathbf{x}) = \sum_{I=1}^{n_p} \mathbf{p}(\mathbf{x}_I - \mathbf{x}) \mathbf{p}^T(\mathbf{x}_I - \mathbf{x}) \phi(\mathbf{x}_I - \mathbf{x}) \quad (58)$$

<sup>339</sup> Taking Eq. (57) back to Eq. (51), the final form of the reproducing kernel shape  
<sup>340</sup> function can be obtained as:

$$\Psi_I(\mathbf{x}) = \mathbf{p}^T(\mathbf{0}) \mathbf{A}^{-1}(\mathbf{x}_I - \mathbf{x}) \phi(\mathbf{x}_I - \mathbf{x}) \quad (59)$$

<sup>341</sup> As shown in Figure 2, reproducing kernel meshfree shape functions are glob-  
<sup>342</sup> ally smooth across the entire domain, using them to discretize the pressure field

343 allows the constraint ratio to be adjusted arbitrarily, without being limited by  
 344 element topology. Meshfree shape functions generally lack the Kronecker delta  
 345 property, which prevents the direct imposition of essential boundary conditions.  
 346 Fortunately, the mixed formulation shown in Eq. 14 only concerns the displace-  
 347 ment essential boundary condition, and this condition can be easily imposed by  
 348 the standard methods, such as the penalty method that used in this work.

349 Moreover, when combined with finite element approximations in Eq. 14,  
 350 numerical integration can be conveniently performed within each finite element  
 351 ( $\Omega_C$ 's). The numerical integration issue caused by the loss of variational con-  
 352 sistency between meshfree shape functions and their derivatives [60] would not  
 353 appear in the mixed formulation of Eq. 14, this is due to the fact that Eq.  
 354 14 solely depends on the meshfree shape functions themselves. Therefore, the  
 355 proposed method employs standard lower-order Gaussian quadrature rules, as  
 356 commonly used in traditional finite element methods, while still maintaining its  
 357 accuracy. Table 2 lists the integration schemes used in this work for mixed-  
 358 formulations. Methods with linear basis functions use an integration scheme of  
 359 order 2. Those with quadratic basis functions use a scheme of order 4. The  
 360 detailed locations and weights of the Gauss points can be found in Ref. [4].

Table 2: Integration schemes for the mixed FE–meshfree formulation

Methods	$n_o$	$n_g$ for $\Omega$	$n_g$ for $\Gamma$
Tri3-RK	2	3	2
Tri6-RK	4	6	3
Quad4-RK	2	$2 \times 2$	2
Quad8-RK	4	$3 \times 3$	3
Tet4-RK	2	4	3
Hex8-RK	2	$2 \times 2 \times 2$	4

$n_o$ : Integration Order    $n_g$ : Number of integration points

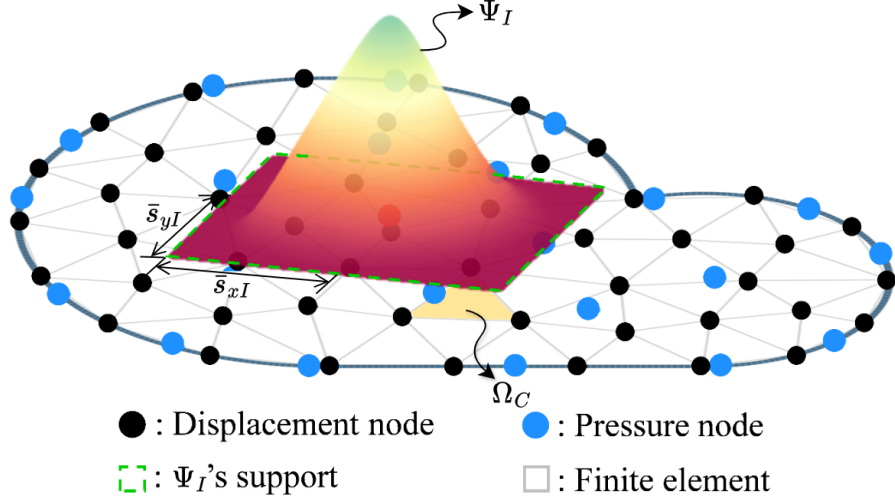


Figure 2: Illustration for reproducing kernel meshfree approximation

361    *4.2. Pressure node distributions with optimal constraint ratio*

362    In this subsection, 2D and 3D inf-sup tests [6], as defined in Eq. 32, are  
363    conducted using the mixed FE-meshfree formulations to validate the proposed  
364    inf-sup value estimator. The 2D test considers the square domain  $\Omega = (0, 1) \times$   
365     $(0, 1)$ , where the displacement is discretized by Tri3 and Quad4 with  $4 \times 4$ ,  
366     $8 \times 8$ ,  $16 \times 16$  and  $32 \times 32$  elements, Tri6 and Quad8 with  $2 \times 2$ ,  $4 \times 4$ ,  $8 \times 8$   
367    and  $16 \times 16$  elements, respectively. The 3D test employs a cube domain  $\Omega =$   
368     $(0, 1) \times (0, 1) \times (0, 1)$  with  $4 \times 4$ ,  $8 \times 8$  and  $16 \times 16$  elements for the Tet4 and Hex8.  
369    For pressure discretization, linear meshfree approximation with a normalized  
370    support size of 1.5 is employed for Tri3, Quad4, Tet4 and Hex8. For Tri6 and  
371    Quad8, a quadratic meshfree approximation with a normalized support size of  
372    2.5 is utilized. In order to avoid the influence of interpolation error, uniform  
373    nodal distributions are used for pressure discretizations, for example in Figure  
374    3, which displays  $4 \times 4$  Quad4 elements with  $4 \times 3$  uniformly distributed pressure  
375    nodes.

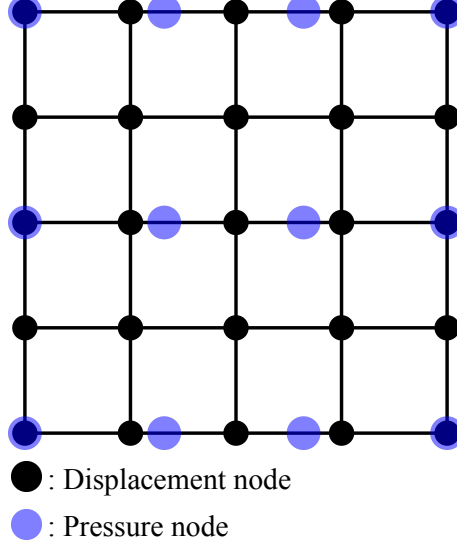


Figure 3: Illustration of uniform nodal distribution for inf-sup test with  $n_u = 5 \times 5$ ,  $n_p = 4 \times 3$

Figures 4–9 show the corresponding results, in which the red line stands for the value of  $\beta$  with respect to the number of pressure nodes  $n_p$ , and the vertical dashed line denotes the stabilized number  $n_s$ . The deeper color of the lines means mesh refinement. The results show that, no matter linear or quadratic elements, as  $n_p$  increases over  $n_s$ , the value of  $\beta$  sharply decreases, and then the inf-sup condition cannot be maintained. This result is consistent with the discussion in Section 3, and again verifies the effect of the proposed estimator.

Moreover, the mixed formulation's results with the traditional optimal constraint ratio  $r = n_d$  are listed in these figures as well, and  $\beta$  in this circumstance is already much smaller than those in the optimal range. Considering the results shown above, the easy programming and efficiency, the pressure nodes are chosen among the displacement nodes. The optimal schemes for linear and quadratic, 2D and 3D element discretizations, namely with  $r = r_{opt}$ , are shown in Figure 10, where every other displacement node is selected as the pressure node. For practical implementations of linear cases, the pressure nodes are initially generated using traditional approaches, such as Delaunay triangulation. Subsequently, the displacement nodes are then obtained through a standard mesh refinement process to the pressure nodes. For quadratic approximations in Tri6 and Quad8 elements, the element vertices are chosen as pressure nodes after displacement element generation. Consequently, all constraint ratios evaluated using the discretizations in Figure 10 fall within the optimal range. The corresponding inf-sup test results for these schemes are also marked in inf-sup test figure and show that, with mesh refinement, their  $\beta$ 's are always maintained at a non-negligible level.

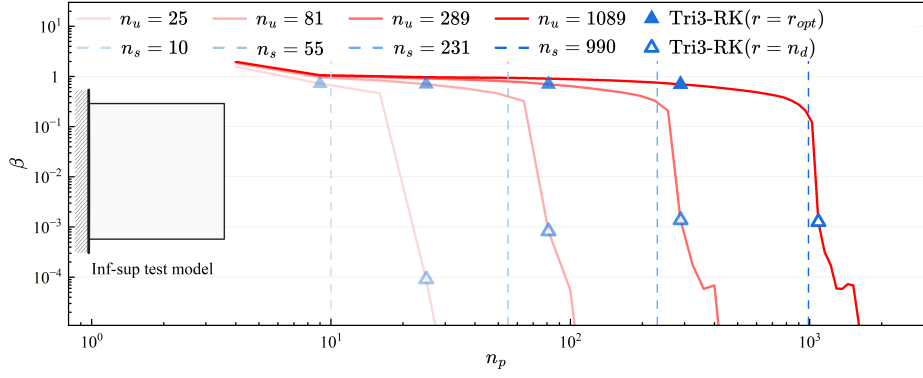


Figure 4: Inf-sup test for Tri3-RK

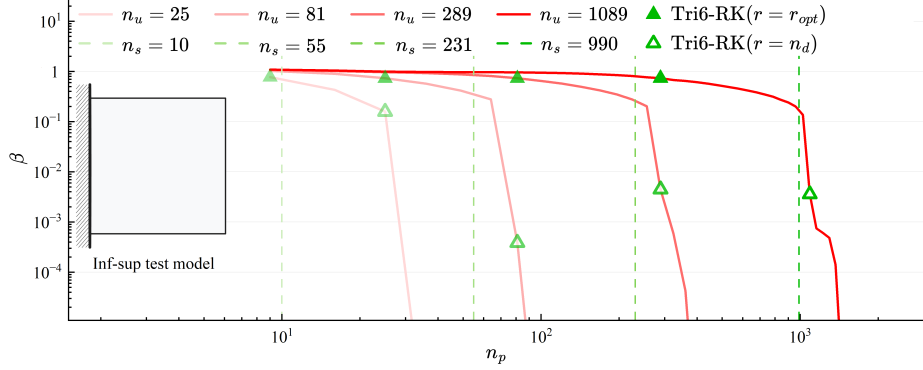


Figure 5: Inf-sup test for Tri6-RK

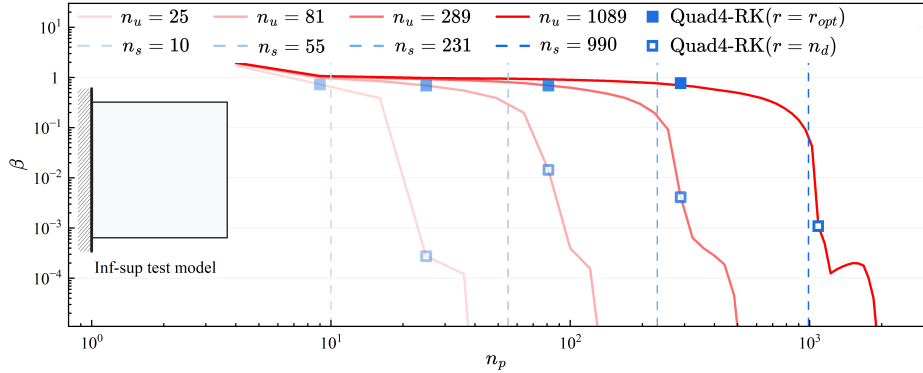


Figure 6: Inf-sup test for Quad4-RK

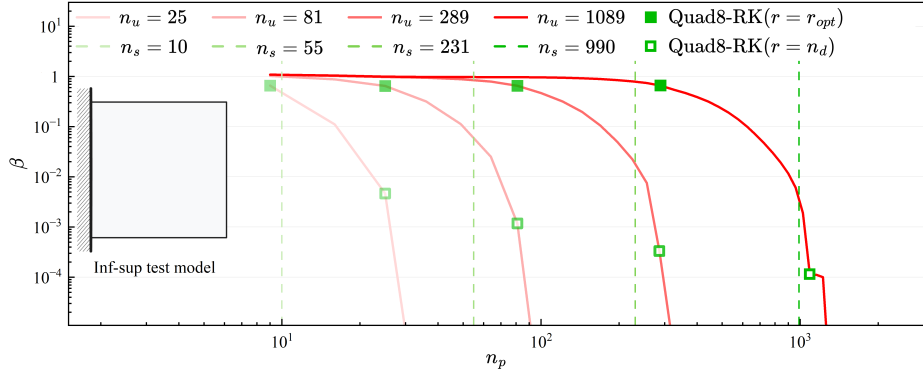


Figure 7: Inf-sup test for Quad8-RK

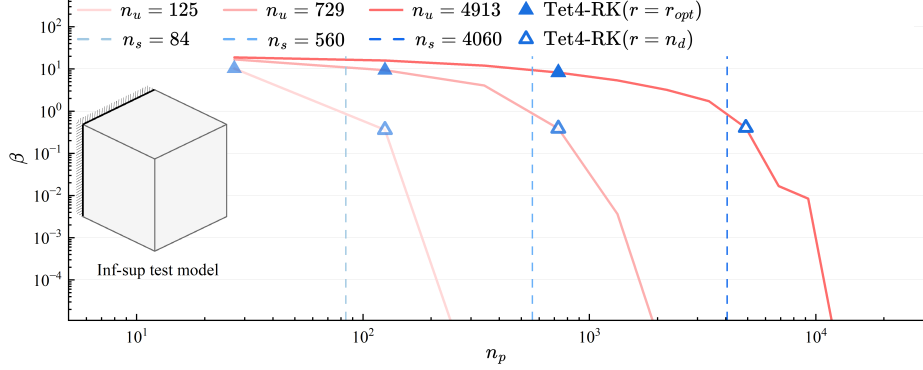


Figure 8: Inf-sup test for Tet4-RK

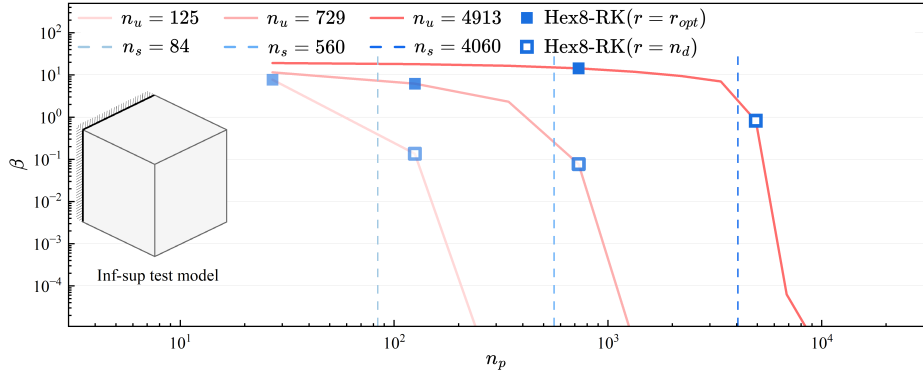


Figure 9: Inf-sup test for Hex8-RK

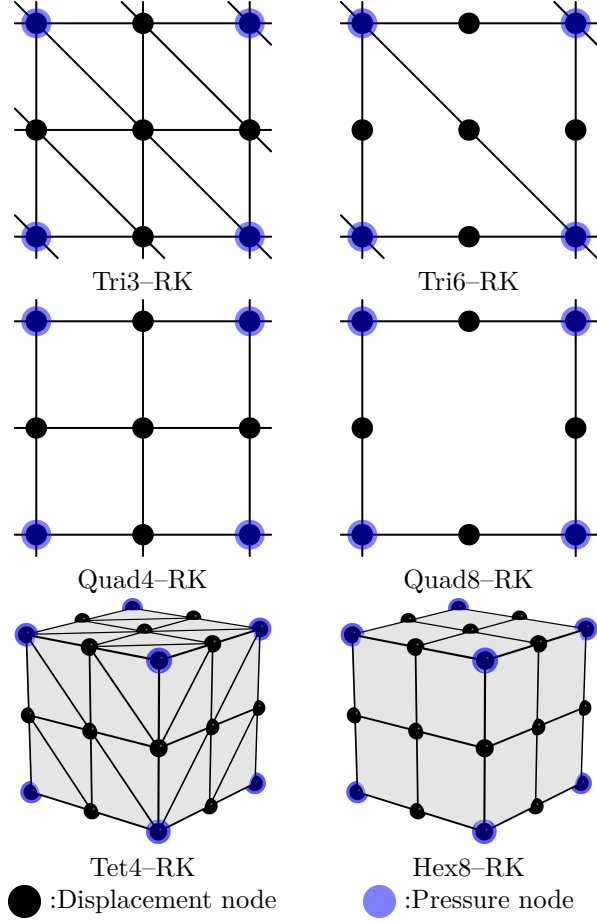


Figure 10: Nodal distribution schemes for mixed FE-meshfree formulations with  $r = r_{opt}$

## 400 5. Numerical examples

### 401 5.1. Cantilever beam problem

402 Consider the cantilever beam problem shown in Figure 11 with length  $L =$   
403  $D = 12$ , and the incompressible material parameters are employed  
404 with Young's modulus  $E = 3 \times 10^6$ , Poisson's ratio  $\nu = 0.5 - 10^{-8}$ . The left hand  
405 side is fixed and the right side subject to a concentrated force  $P = 1000$ . All  
406 the prescribed values in the boundary conditions are evaluated by the analytical  
407 solution that is given as follows [61]:

$$\begin{cases} u_x(\mathbf{x}) = -\frac{Py}{6EI} \left( (6L - 3x)x + (2 + \bar{\nu})(y^2 - \frac{D^2}{4}) \right) \\ u_y(\mathbf{x}) = \frac{P}{6EI} \left( 3\bar{\nu}y^2(L - x) + (4 + 5\bar{\nu})\frac{D^2x}{4} + (3L - x)x^2 \right) \end{cases} \quad (60)$$

408 where  $I$  is the beam's moment of inertia,  $\bar{E}$  and  $\bar{\nu}$  are the material parameters  
 409 for plane strain hypothesis, they can be expressed by:

$$I = \frac{D^3}{12}, \quad \bar{E} = \frac{E}{1 - \nu^2}, \quad \bar{\nu} = \frac{\nu}{1 - \nu} \quad (61)$$

410 And correspondingly, the stress components and the pressure are evaluated by

$$\begin{cases} \sigma_{xx} = -\frac{P(L-x)y}{I} \\ \sigma_{yy} = 0 \\ \sigma_{xy} = \frac{P}{2I}\left(\frac{D^2}{4} - y^2\right) \\ p = -\frac{P(1+\nu)(L-x)y}{3I} \end{cases} \quad (62)$$

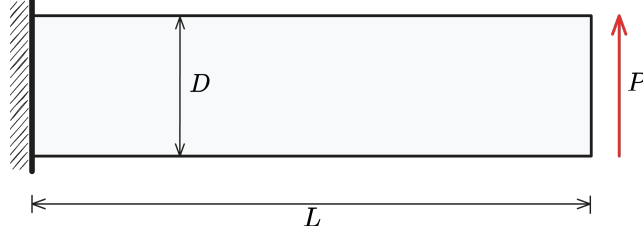


Figure 11: Illustration of cantilever beam problem

411 In this problem, the Tri3, Quad4 elements with  $16 \times 4$ ,  $32 \times 8$ ,  $64 \times 16$ ,  $128 \times 32$   
 412 grids, and Tri6, Quad8 elements with  $8 \times 2$ ,  $16 \times 4$ ,  $32 \times 8$ ,  $64 \times 16$  grids are  
 413 employed for displacement discretization. The pressure is discretized by linear  
 414 and quadratic meshfree approximations with 1.5 and 2.5 characterized support  
 415 sizes respectively. The strain and pressure errors with respect to pressure nodes  
 416  $n_p$  are displayed in Figures 12, 13, where, to avoid the interpolation error, the  
 417 pressure nodes are uniformly distributed independent with displacement nodes  
 418 by the same way in Section 4.2. The vertical dashed lines stand for the stabilized  
 419 number  $n_s$ . The figures imply that all pressure errors immediately increase when  
 420 their constraint ratios are out of the optimal range, and quadratic elements still  
 421 have better results than linear elements. As  $n_p$  becomes very small, the pressure  
 422 errors do not increase. This is because the pressure error estimator in Eq. (A.14)  
 423 is primarily controlled by the strain error and the inf-sup value  $\beta$ . The exact  
 424 pressure solution in Eq. (62) is only a second-order polynomial. As a result, the  
 425 pressure interpolation error in Eq. (A.14) is either very small or nonexistent.  
 426 For the strain error, the Quad8-RK method shows stable results regardless of  
 427 whether the constraint ratio is in the optimal range. This may be due to the  
 428 fact that the Quad8 element with a regular mesh satisfies the relationship of  
 429 Eq. (A.16). In this context, the strain error of Eq. (A.10) is independent of the  
 430 inf-sup value  $\beta$  and remains at a low level.

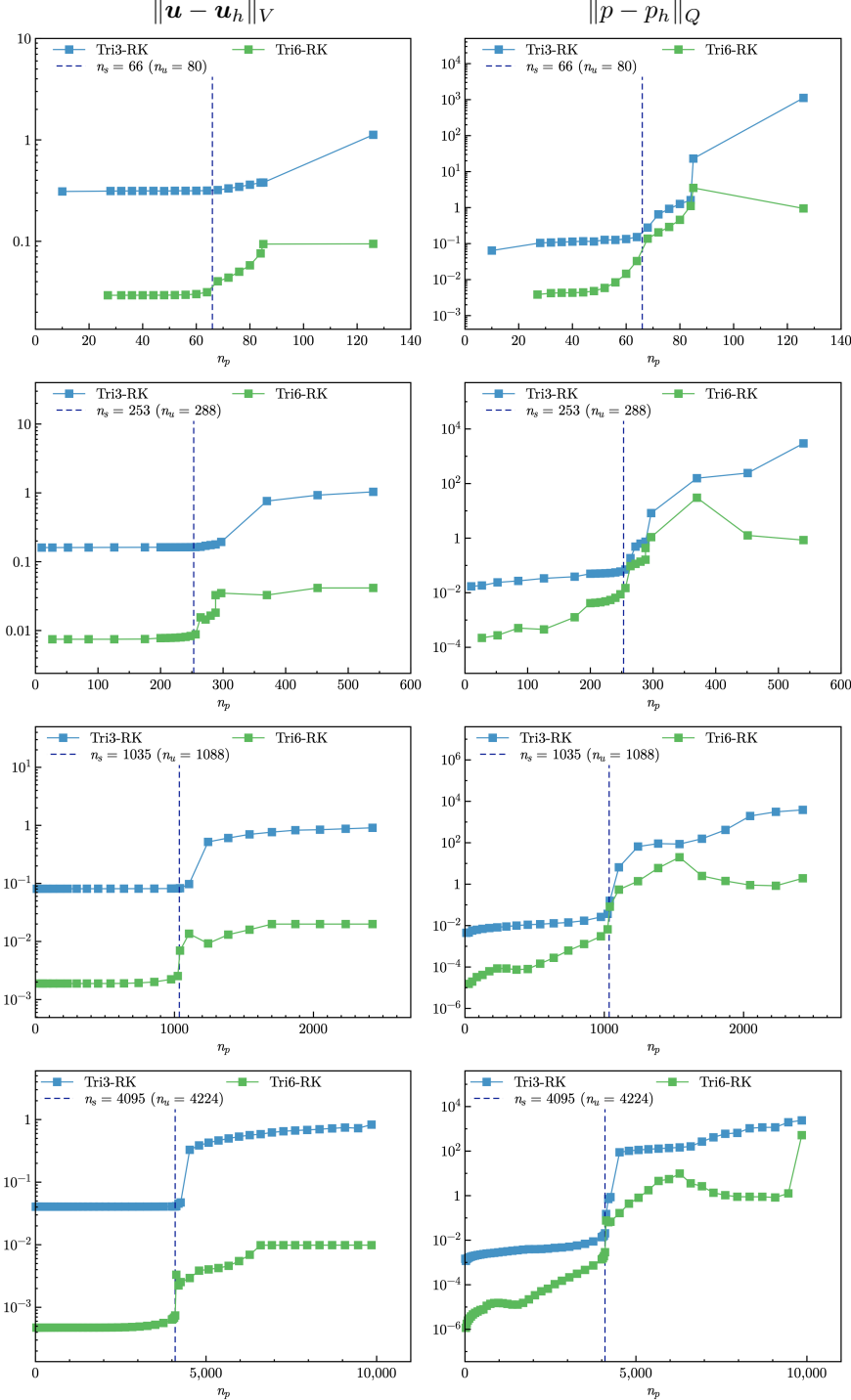


Figure 12: Strain and pressure errors vs.  $n_p$  for cantilever beam problem with triangular elements

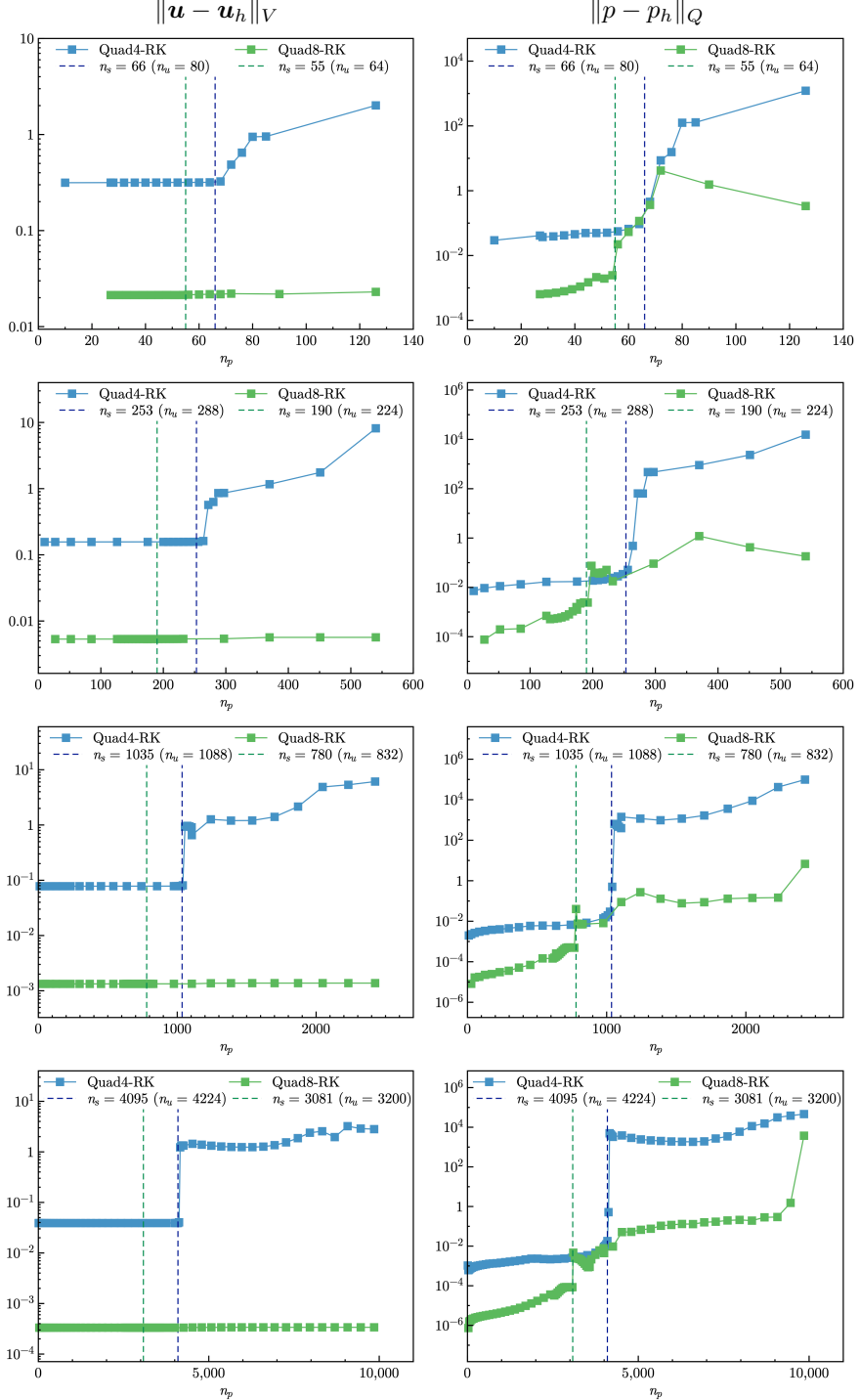


Figure 13: Strain and pressure errors vs.  $n_p$  for cantilever beam problem with quadrilateral elements

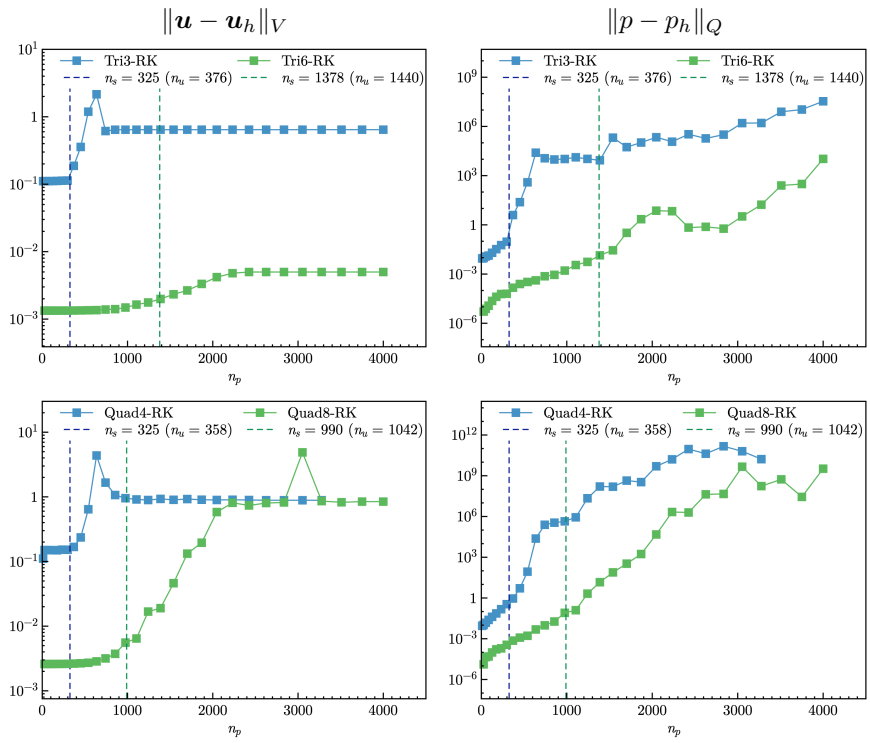


Figure 14: Strain and pressure errors vs.  $n_p$  for cantilever beam problem with non-uniform elements

Figures 15, 16 are the strain and pressure error convergence studies for triangular and quadrilateral elements, respectively, in which Tri3–RK, Tri6–RK with  $r = n_d$ , the MINI element [32], 6–node triangular displacement element with 3–node continuous triangular pressure element (T6C3) are the comparative methods for Tri3–RK and Tri6–RK with  $r = r_{opt}$ , and Quad4–RK, Quad8–RK with  $r = n_d$ , 4–node quadrilateral displacement element with 1–node piecewise constant pressure (Q4P1), 8–node quadrilateral displacement element with 3–node piecewise linear pressure (Q8P3) are employed for comparison with Quad4–RK and Quad8–RK with  $r = r_{opt}$ . Except Tri3–RK, Quad8–RK with  $r = n_d$  for strain error, all formulations with the traditional constraint ratio of  $r = n_d$  cannot ensure the optimal error convergence rates. The proposed mixed formulations with  $r = r_{opt}$  can maintain the optimal error convergence ratio, except the strain error of Quad8–RK is a little larger than that of Q8P3, the proposed approaches show the best performance in accuracy.

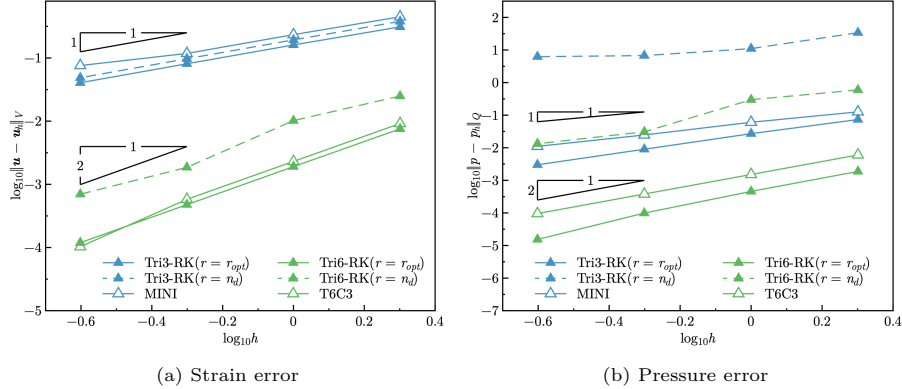


Figure 15: Error convergence study for cantilever beam problem with triangular elements

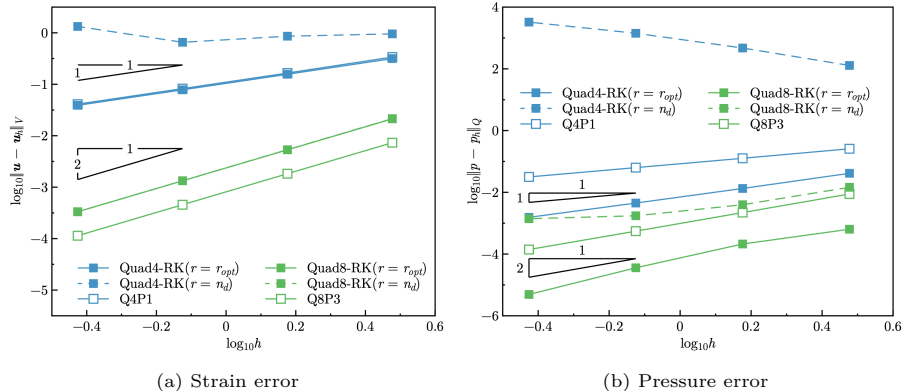


Figure 16: Error convergence study for cantilever beam problem with quadrilateral elements

445    5.2. Plate with hole problem

446    Consider an infinite plate with a hole centered at the origin, as shown in  
 447    Figure 17, and at the infinity towards the  $x$ -direction subjected to a uniform  
 448    traction  $T = 1000$ . The geometric and material parameters for this problem are  
 449    that the ratio of the hole  $a = 1$ , Young's modulus  $E = 3 \times 10^6$ , and Poisson's  
 450    ratio  $\nu = 0.5 - 10^{-8}$ . The analytical solution of this problem refers to the  
 451    Michell solution [61] as:

$$\begin{cases} u_x(\rho, \theta) = \frac{T a}{8\mu} \left( \frac{\rho}{a} (k+1) \cos \theta - \frac{2a^3}{\rho^3} \cos 3\theta + \frac{2a}{\rho} ((1+k) \cos \theta + \cos 3\theta) \right) \\ u_y(\rho, \theta) = \frac{T a}{8\mu} \left( \frac{\rho}{a} (k-3) \sin \theta - \frac{2a^3}{\rho^3} \sin 3\theta + \frac{2a}{\rho} ((1-k) \sin \theta + \sin 3\theta) \right) \end{cases} \quad (63)$$

452    in which  $k = \frac{3-\nu}{1+\nu}$ ,  $\mu = \frac{E}{2(1+\nu)}$ . And the stress components are given by:

$$\begin{cases} \sigma_{xx} = T \left( 1 - \frac{a^2}{\rho^2} \left( \frac{3}{2} \cos 2\theta + \cos 4\theta \right) + \frac{3a^4}{2\rho^4} \cos 4\theta \right) \\ \sigma_{yy} = -T \left( \frac{a^2}{\rho^2} \left( \frac{1}{2} \cos 2\theta - \cos 4\theta \right) + \frac{3a^4}{2\rho^4} \cos 4\theta \right) \\ \sigma_{xy} = -T \left( \frac{a^2}{\rho^2} \left( \frac{1}{2} \sin 2\theta + \sin 4\theta \right) - \frac{3a^4}{2\rho^4} \sin 4\theta \right) \end{cases} \quad (64)$$

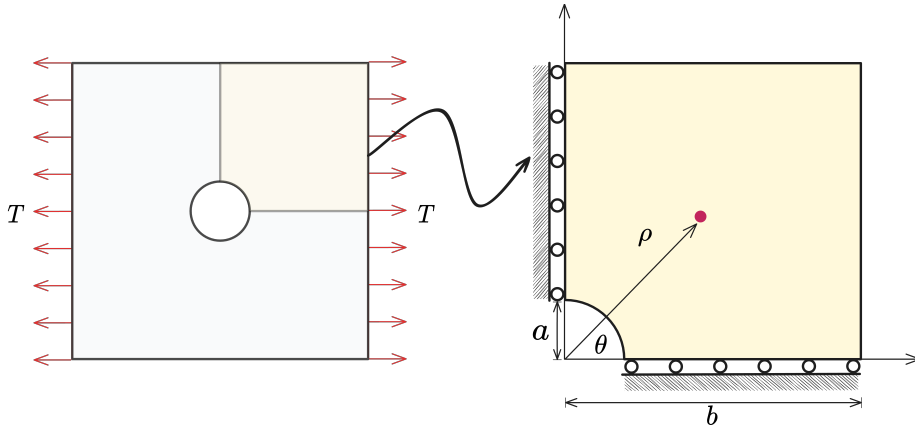


Figure 17: Illustration of plate with hole problem

453    According to the symmetry property of this problem, only a quarter model  
 454    with length  $b = 5$  is considered as shown in Figure 17. The displacement is  
 455    discretized by 3-node, 6-node triangular elements, 4-node and 8-node quadrilater-  
 456    al elements. The corresponding linear and quadratic meshfree formulations  
 457    are employed for pressure discretization, and the characterized support sizes  
 458    are chosen as 1.5 and 2.5, respectively. Figures 18, 19 study the relationship

459 between strain, pressure errors, and  $n_p$  using the nodal distributions uniformly  
460 related to displacement nodes. Unlike the quadrilateral element case in Section  
461 5.1, both displacement and pressure errors in this problem increase as  $n_p$  reduces  
462 to a small value. Tri3–RK exhibits less sensitivity in strain error than Tri6–RK.  
463 This may be because, as shown in Eqs. (A.10) and (A.20), the displacement  
464 approximation error for the space of  $\ker \mathcal{P}_h$  does not increase as immediately  
465 when  $\frac{C_p}{\beta}$  in Eq. (A.20) is not too much larger than 1. However, its error in-  
466 creases as  $n_p$  goes up. Both FE–RK with constraint ratios under the optimal  
467 range perform acceptably.

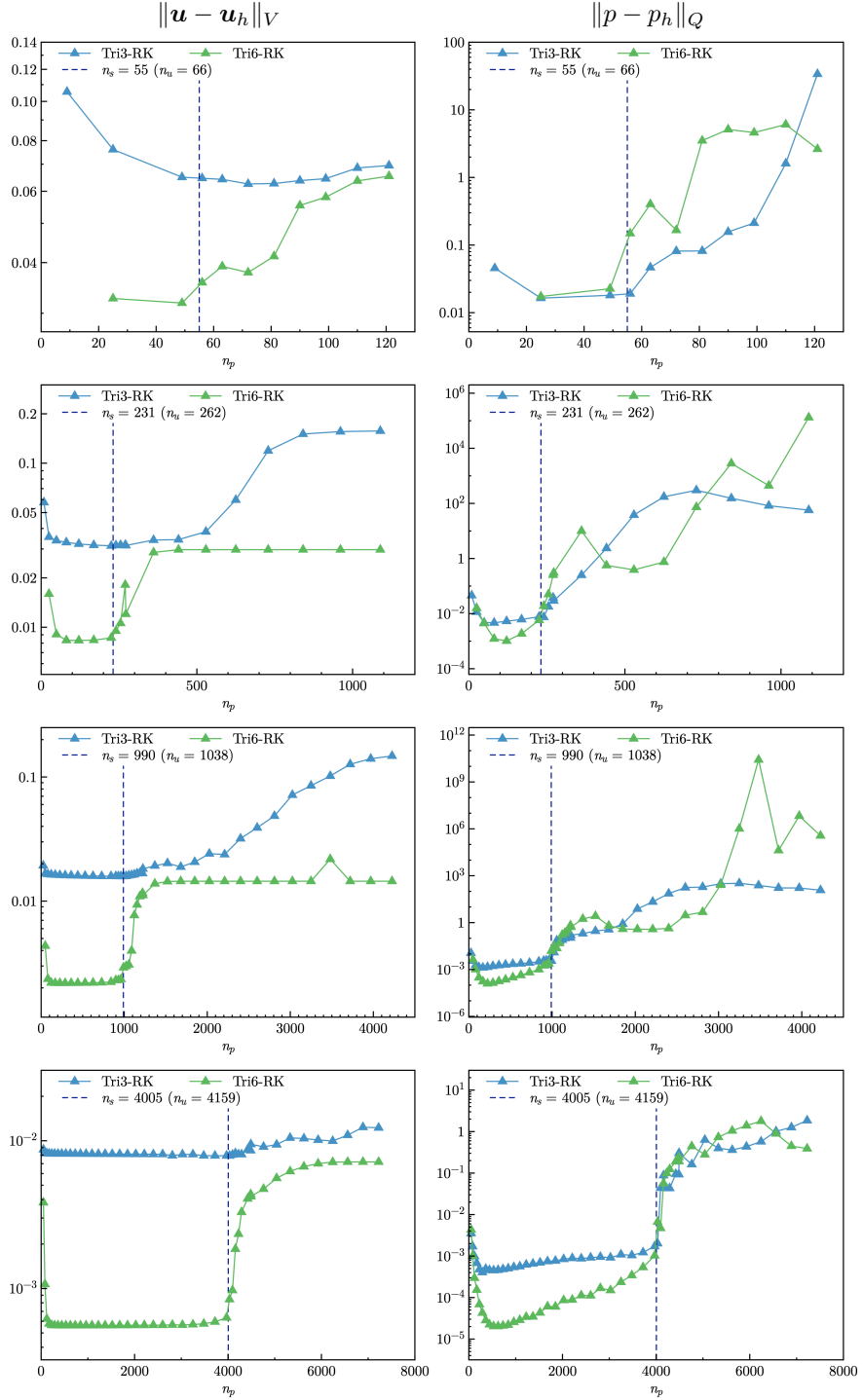


Figure 18: Strain and pressure errors vs.  $n_p$  for plate with hole problem

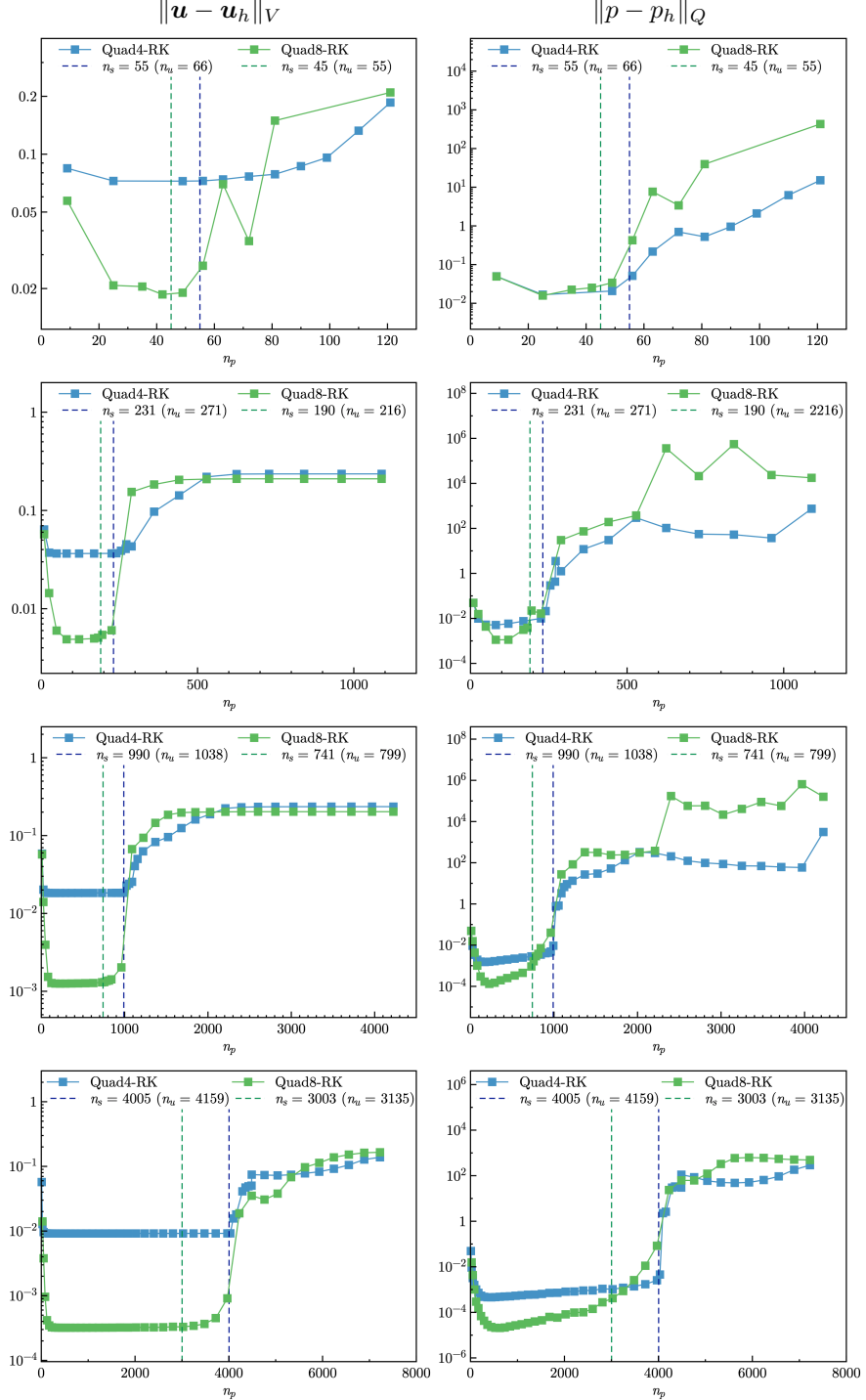


Figure 19: Strain and pressure errors vs.  $n_p$  for plate with hole problem

468 The corresponding error convergence studies are presented in Figures 20, 21,  
 469 the results show that only Tri3–RK with  $r = 2$  shows a comparable result with  
 470 the optimal one with  $r = r_{opt}$  in strain error. The other formulations with the  
 471 traditional constraint ratio show lower accuracy and error convergence rates.

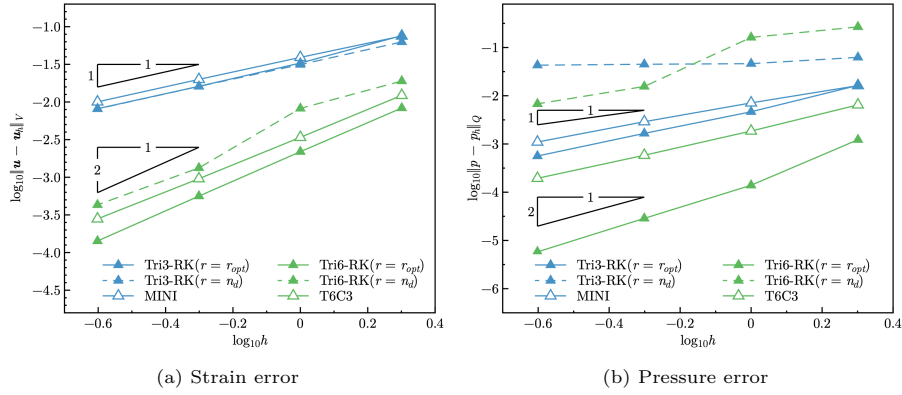


Figure 20: Error convergence study for plate with a hole problem with triangular elements

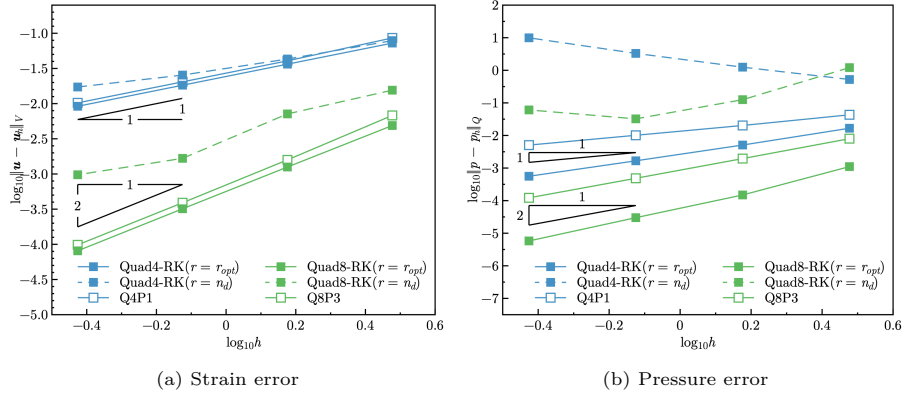


Figure 21: Error convergence study for plate with a hole problem with quadrilateral elements

472 Furthermore, the influence of the integration scheme for this problem is  
 473 investigated. As shown in Tables 3 and 4, the integration order  $n_o$  is varied  
 474 from 1 to 5 for triangular elements and from 1 to 11 for quadrilateral elements.  
 475 The results show that the proposed mixed formulations are not sensitive to the  
 476 integration order. Using the traditional lower-order Gauss integration scheme  
 477 can sufficiently obtain accurate results. This is consistent with the previous  
 478 analysis in Section 4.1.

Table 3: Error comparison with different triangular integration schemes for plate with a hole problem

$n_o$	$n_g$ for $\Omega$	$n_g$ for $\Gamma$	Tri3-RK		Tri6-RK	
			$\ \mathbf{u} - \mathbf{u}_h\ _V$	$\ p - p_h\ _Q$	$\ \mathbf{u} - \mathbf{u}_h\ _V$	$\ p - p_h\ _Q$
1	1	1	3.11E-2	3.53E-3	8.53E17	1.31E4
2	3	2	3.11E-2	3.67E-3	8.33E-3	1.20E-3
3	4	2	3.11E-2	3.67E-3	8.32E-3	1.20E-3
4	6	3	3.11E-2	3.68E-3	8.32E-3	1.22E-3
5	7	3	3.11E-2	3.68E-3	8.32E-3	1.22E-3

$n_o$ : Integration order  $n_g$ : Number of integration points

Table 4: Error comparison with different quadrilateral integration schemes for plate with a hole problem

$n_o$	$n_g$ for $\Omega$	$n_g$ for $\Gamma$	Quad4-RK		Quad8-RK	
			$\ \mathbf{u} - \mathbf{u}_h\ _V$	$\ p - p_h\ _Q$	$\ \mathbf{u} - \mathbf{u}_h\ _V$	$\ p - p_h\ _Q$
1	3	1	3.64E-2	5.01E-3	9.53E13	8.15E-1
3	$2 \times 2$	2	3.64E-2	5.09E-3	4.33E-2	8.84E-3
5	$3 \times 3$	3	3.62E-2	3.71E-3	1.27E-3	4.42E-5
7	$4 \times 4$	4	3.62E-2	3.70E-3	1.26E-3	1.49E-4
9	$5 \times 5$	5	3.62E-2	3.70E-3	1.26E-3	1.50E-4
11	$6 \times 6$	6	3.62E-2	3.70E-3	1.26E-3	1.50E-4

$n_o$ : Integration Order  $n_g$ : Number of integration points

### 5.3. Cook's membrane problem

The Cook's membrane problem [12] is used herein for stability analysis of pressure. The geometry of this problem is shown in Figure 22, in which the left hand side is fixed and the right hand side subjects a concentrated force  $P = 6.25$  in the  $y$ -direction. The material parameters are Young's modulus  $E = 70.0$  and Poisson's ratio  $\nu = 0.5 - 10^{-8}$ .

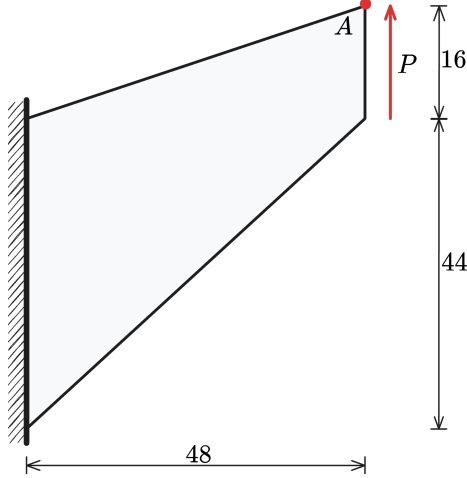


Figure 22: Illustration of Cook's membrane problem

In this test, we evaluated the convergence properties by comparing the vertical displacement at point  $A$  against a reference value of 28.0. As shown in Figure 23 illustrates, the methods employing  $r = r_{opt}$  produced results that were notably closer to this reference value than those using  $r = n_d$ . Furthermore, to investigate stability, Figures 24–27 show the pressure contour plots for non-uniform Tri3–RK, Tri6–RK, Quad4–RK, and Quad8–RK formulations with  $r = n_d$  and  $r = r_{opt}$ , respectively. The reproducing kernel meshfree approximations are employed for pressure discretization with characterized support sizes of 1.5 for the linear basis function and 2.5 for the quadratic basis function. The results imply that the pressure contour plots with the optimal constraint ratio  $r = r_{opt}$  show a more stable and smooth pressure distribution compared to those with the traditional constraint ratio  $r = n_d$ .

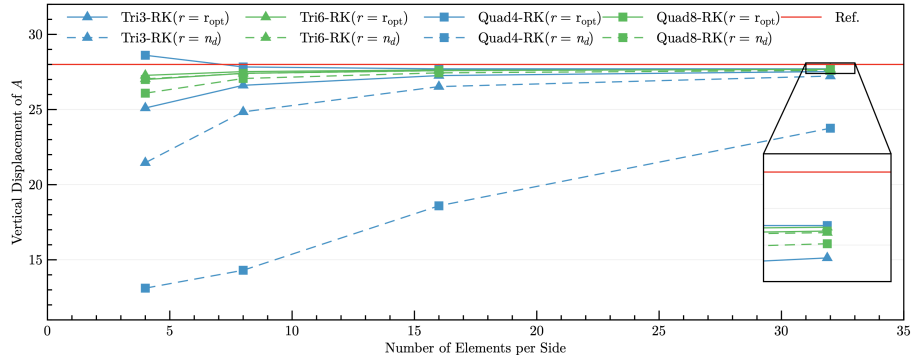


Figure 23: Convergence comparison of the vertical displacement at point  $A$  for Cook's membrane problem

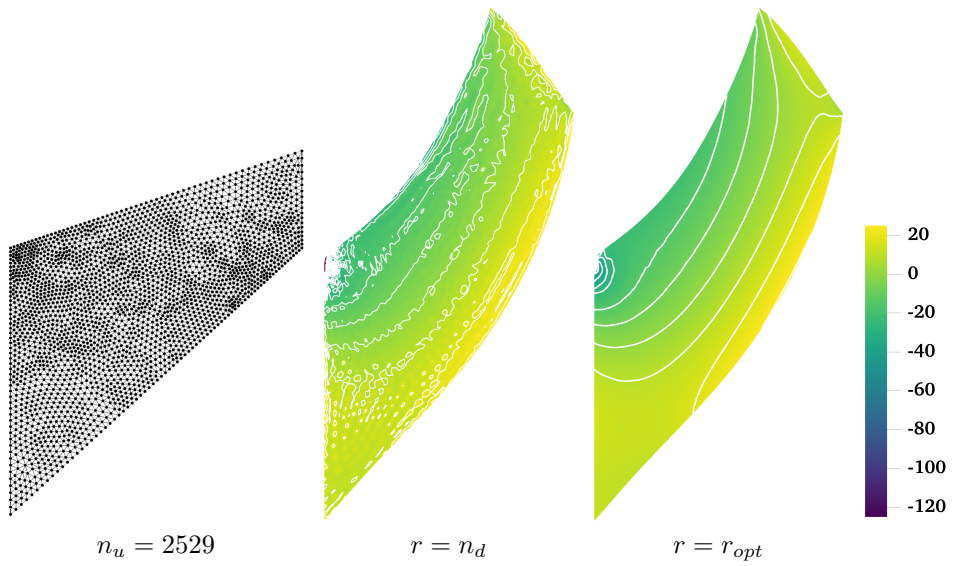


Figure 24: Pressure contour plots for Cook's membrane problem using Tri3–RK

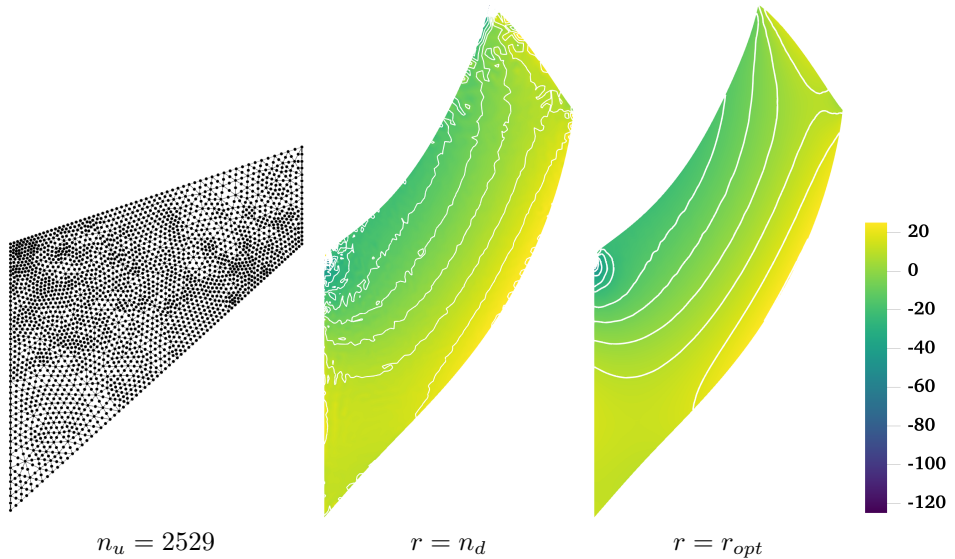


Figure 25: Comparison of pressure contour plots for Cook's membrane problem using Tri6–RK

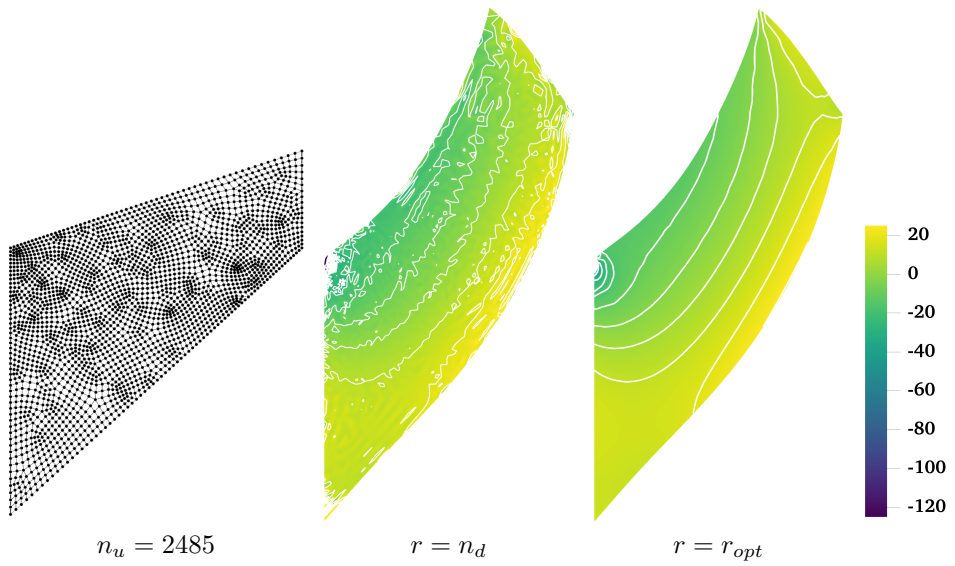


Figure 26: Comparison of pressure contour plots for Cook's membrane problem using Quad4-RK

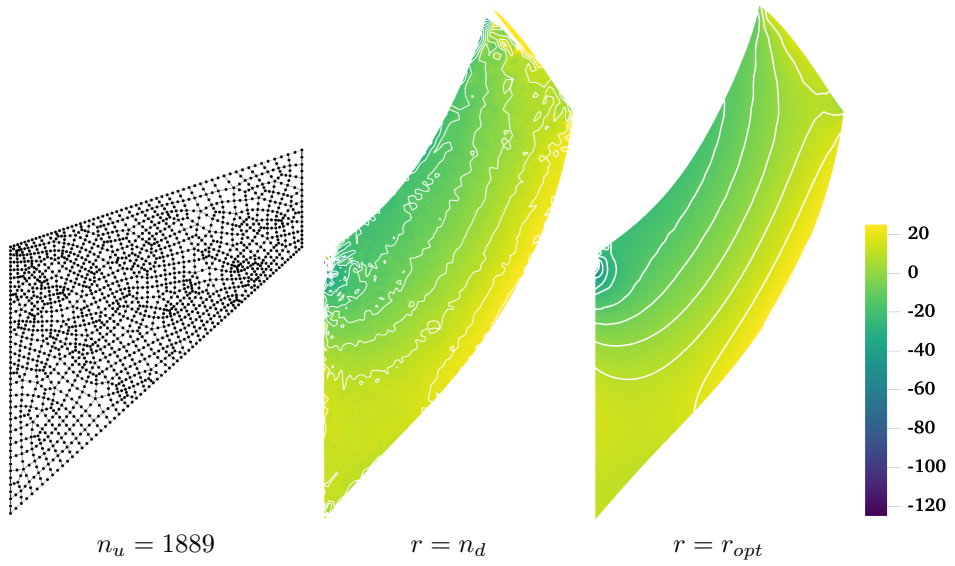


Figure 27: Comparison of pressure contour plots for Cook's membrane problem using Quad8-RK

Table 5: Condition number and efficiency comparison for Cook's membrane problem

Method	Condition number	CPU-time (s) for		
		Shape function	Assembly	Solving
MINI	1.11E06	0.025	0.327	0.022
Tri3-RK( $r = n_d$ )	1.89E10	1.73	4.160	0.108
Tri3-RK( $r = r_{opt}$ )	1.13E08	1.290	1.720	0.052
T6P3	1.62E05	0.004	0.380	0.021
Tri6-RK( $r = n_d$ )	2.48E16	1.62	1.67	0.294
Tri6-RK( $r = r_{opt}$ )	3.69E10	1.110	0.634	0.077
Q4P1	5.75E12	0.011	0.344	0.021
Quad4-RK( $r = n_d$ )	5.21E10	2.1	4.89	0.122
Quad4-RK( $r = r_{opt}$ )	1.97E08	1.5	2.14	0.057
Q8P3	2.69E07	0.005	0.373	0.015
Quad8-RK( $r = n_d$ )	2.75E15	1.17	1.18	0.184
Quad8-RK( $r = r_{opt}$ )	8.67E10	0.847	0.471	0.065

#### 5.4. Block under compression problem

The incompressible block problem [62] shown in Figure 28 is considered for testing 3D mixed formulations. The block's dimensions are  $2L \times 2L \times L$ ,  $L = 1$ . At the center of the top surface of the block is applied a pressure load  $P$  with the area of  $L \times L$ . Due to the symmetry of this problem, only a quarter model is considered. The Young's modulus and Poisson's ratio are set as  $E = 240.56839$  and  $\nu = 0.5 - 10^{-8}$ , respectively.

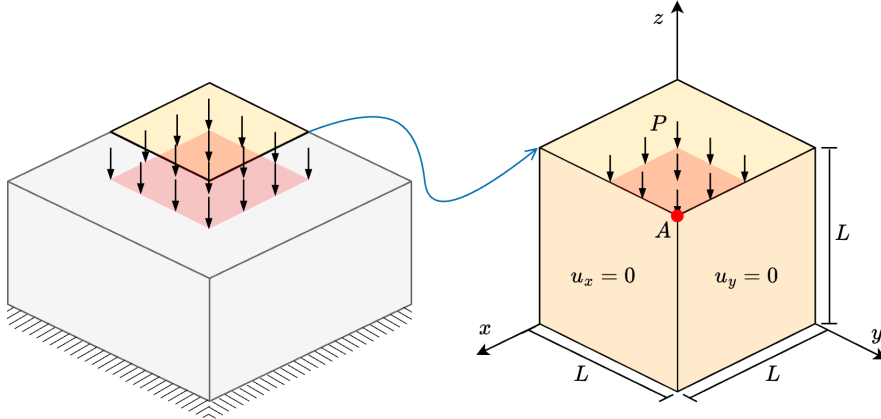


Figure 28: Illustration of block under compression problem

The convergence properties of the mixed formulations are evaluated by comparing the compression level at point  $A$  under various loading conditions  $P/P_0$ , where  $P_0 = 4$ . As shown in Figure 29, all the results exhibit good convergence behavior across different loading levels. Figures 30, 31 study the pressure

508 stability of 3D mixed FE-meshfree formulations, Tet4-RK and Hex8-RK, with  
 509 non-uniform nodal distribution, while the pressure is discretized by linear mesh-  
 510 free approximations with a characterized support size of 1.5. The corresponding  
 511 results also show the well performance of the proposed optimal constraint ratio  
 512  $r = r_{opt}$ . The mixed formulations with the traditional constraint ratio  $r = n_d$   
 513 show comparable displacement results, but exhibit significant pressure instabil-  
 514 ity.

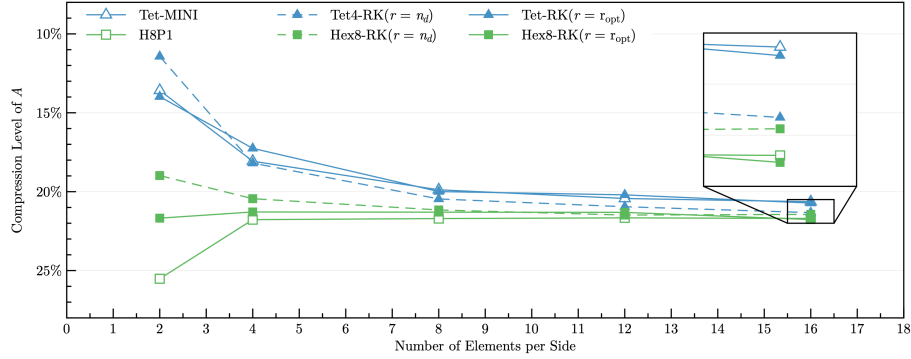


Figure 29: Convergence comparison of compression level (%) at point A for block under compression problem

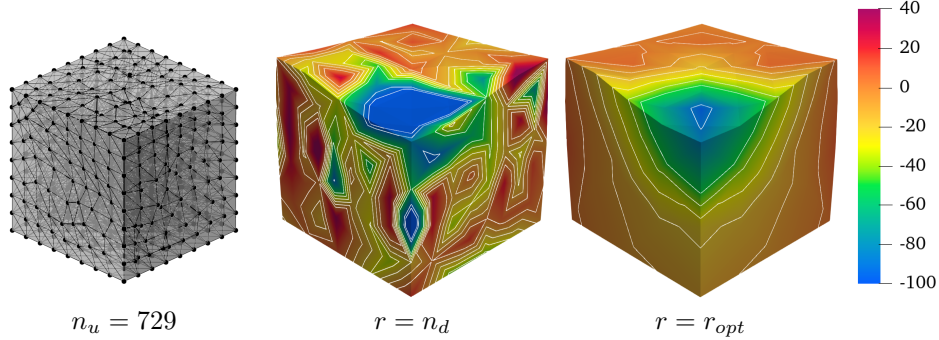


Figure 30: Comparison of pressure contour plots for block under compression problem using Tet4-RK

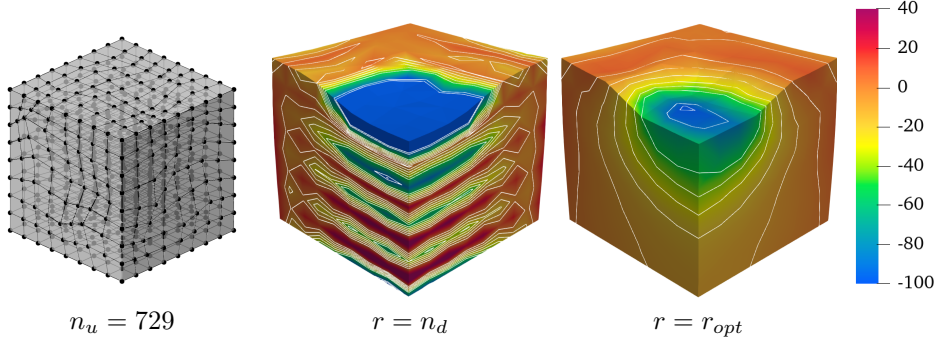


Figure 31: Comparison of pressure contour plots for block under compression problem using Hex8–RK

## 515 6. Conclusion

516 This paper proposes a novel optimal constraint ratio derived from the inf–sup  
 517 condition to address volumetric locking. The optimal constraint ratio requires  
 518 that, for a given number of displacement DOFs, the number of pressure DOFs  
 519 should remain below a stabilized number determined by the proposed inf–sup  
 520 value estimator. For a well-posed nodal distribution, simply counting the dis-  
 521 placement and pressure DOFs can determine whether the formulation satisfies  
 522 the inf–sup condition. Compared to the traditional constraint ratio, the pro-  
 523 posed ratio is theoretically grounded in the inf–sup condition and thus is more  
 524 precise.

525 To implement this constraint ratio, a mixed finite element (FE) and meshfree  
 526 formulation is developed. Displacements are discretized using 3-node and 6-node  
 527 triangular elements, 4-node and 8-node quadrilateral elements in 2D, and 4-node  
 528 tetrahedral and 8-node hexahedral elements in 3D. Correspondingly, linear and  
 529 quadratic reproducing kernel meshfree approximations are used for pressure  
 530 discretization. The reproducing kernel approximation equips globally smooth  
 531 shape functions, allowing arbitrary pressure DOF placement without the limit  
 532 of element.

533 Inf–sup tests for mixed FE–meshfree formulations with different constraint  
 534 ratios verify the effectiveness of the proposed inf–sup value estimator. For effi-  
 535 ciency and ease of implementation, the final nodal distribution scheme selects  
 536 every other displacement node as a pressure node, ensuring the optimal con-  
 537 straint ratio and satisfying the inf–sup condition.

538 A series of 2D and 3D incompressible elasticity examples demonstrate the  
 539 effectiveness of the proposed mixed formulation. Results show that formulations  
 540 with the optimal constraint ratio yield accurate displacement and pressure solu-  
 541 tions. When the constraint ratio exceeds the optimal value, errors rise sharply  
 542 to unacceptable levels, with the 8-node quadrilateral element being the only  
 543 exception that maintains good displacement accuracy. Error convergence stud-  
 544 ies and pressure contour plots further confirm that mixed formulations with

545 the optimal constraint ratio achieve optimal convergence rates and effectively  
546 suppress pressure oscillations.

547 **Acknowledgment**

548 The support of this work by the National Natural Science Foundation of  
549 China (12102138), the Natural Science Foundation of Fujian Province of China  
550 (2023J01108) and the Fundamental Research Funds of Central Universities  
551 (ZQN-1014) is gratefully acknowledged.

552 **References**

- 553 [1] F. Brezzi, M. Fortin, Mixed and Hybrid Finite Element Methods, Vol. 15 of  
554 Springer Series in Computational Mathematics, Springer, New York, NY,  
555 1991.
- 556 [2] T. J. Hughes, The Finite Element Method: Linear Static and Dynamic  
557 Finite Element Analysis, Prentice Hall, New Jersey, 2000.
- 558 [3] I. Babuška, R. Narasimhan, The Babuška-Brezzi condition and the patch  
559 test: An example, Computer Methods in Applied Mechanics and Engineering  
560 140 (1-2) (1997) 183–199.
- 561 [4] K. J. Bathe, Finite Element Procedures, Prentice Hall, Englewood Cliffs,  
562 New Jersey, 1996.
- 563 [5] D. S. Malkus, Eigenproblems associated with the discrete LBB condition for  
564 incompressible finite elements, International Journal of Engineering Science  
565 19 (10) (1981) 1299–1310.
- 566 [6] D. Chapelle, K. J. Bathe, The inf-sup test, Computers & Structures 47 (4)  
567 (1993) 537–545.
- 568 [7] F. Brezzi, K. J. Bathe, Studies of finite element procedures the inf-sup  
569 condition equivalent forms and applications.
- 570 [8] D. Gallistl, Rayleigh-Ritz approximation of the inf-sup constant for the  
571 divergence, Mathematics of Computation 88 (315) (2019) 73–89.
- 572 [9] P. Hood, C. Taylor, Navier-Stokes equations using mixed interpolation,  
573 Finite element methods in flow problems (1974) 121–132.
- 574 [10] D. S. Malkus, T. J. Hughes, Mixed finite element methods - Reduced and  
575 selective integration techniques: A unification of concepts, Computer Meth-  
576 ods in Applied Mechanics and Engineering 15 (1) (1978) 63–81.
- 577 [11] T. Shilt, R. Deshmukh, J. J. McNamara, P. J. O’Hara, Solution of nearly  
578 incompressible field problems using a generalized finite element approach,  
579 Computer Methods in Applied Mechanics and Engineering 368 (2020)  
580 113165.

- 581 [12] J. C. Simo, M. S. Rifai, A class of mixed assumed strain methods and  
 582 the method of incompatible modes, International Journal for Numerical  
 583 Methods in Engineering 29 (8) (1990) 1595–1638.
- 584 [13] M. Broccardo, M. Micheloni, P. Krysl, Assumed-deformation gradient finite  
 585 elements with nodal integration for nearly incompressible large deformation  
 586 analysis, International Journal for Numerical Methods in Engineering 78 (9) (2009) 1113–1134.
- 588 [14] W. M. Coombs, T. J. Charlton, M. Cortis, C. E. Augarde, Overcoming vol-  
 589 umetric locking in material point methods, Computer Methods in Applied  
 590 Mechanics and Engineering 333 (2018) 1–21.
- 591 [15] S. Saloustros, M. Cervera, S. Kim, M. Chiumenti, Accurate and locking-free  
 592 analysis of beams, plates and shells using solid elements, Computational  
 593 Mechanics 67 (2021) 883–914.
- 594 [16] J. Simo, R. Taylor, K. Pister, Variational and projection methods for the  
 595 volume constraint in finite deformation elasto-plasticity, Computer Meth-  
 596 ods in Applied Mechanics and Engineering 51 (1-3) (1985) 177–208.
- 597 [17] C. R. Dohrmann, P. B. Bochev, A stabilized finite element method for the  
 598 Stokes problem based on polynomial pressure projections, International  
 599 Journal for Numerical Methods in Fluids 46 (2) (2004) 183–201.
- 600 [18] A. Valverde-González, J. Reinoso, B. Dortdivanlioglu, M. Paggi, Locking  
 601 treatment of penalty-based gradient-enhanced damage formulation for fail-  
 602 ure of compressible and nearly incompressible hyperelastic materials, Com-  
 603 putational Mechanics 72 (2023) 635–662.
- 604 [19] B.-B. Xu, F. Peng, P. Wriggers, Stabilization-free virtual element method  
 605 for finite strain applications, Computer Methods in Applied Mechanics and  
 606 Engineering 417 (2023) 116555.
- 607 [20] F. S. Liguori, A. Madeo, S. Marfia, G. Garcea, E. Sacco, A stabilization-  
 608 free hybrid virtual element formulation for the accurate analysis of 2D  
 609 elasto-plastic problems, Computer Methods in Applied Mechanics and En-  
 610 gineering 431 (2024) 117281.
- 611 [21] R. Alves de Sousa, R. Natal Jorge, R. Fontes Valente, J. César de Sá, A new  
 612 volumetric and shear locking-free 3D enhanced strain element, Engineering  
 613 Computations 20 (7) (2003) 896–925.
- 614 [22] K.-J. Bathe, The inf-sup condition and its evaluation for mixed finite ele-  
 615 ment methods, Computers & Structures 79 (2) (2001) 243–252.
- 616 [23] T. J. R. Hughes, Multiscale phenomena: Green's functions, the Dirichlet-  
 617 to-Neumann formulation, subgrid scale models, bubbles and the origins of  
 618 stabilized methods, Computer Methods in Applied Mechanics and Engi-  
 619 neering 127 (1) (1995) 387–401.

- 620 [24] R. Rossi, R. Zorrilla, R. Codina, A stabilised displacement-volumetric  
 621 strain formulation for nearly incompressible and anisotropic materials,  
 622 Computer Methods in Applied Mechanics and Engineering 377 (2021)  
 623 113701.
- 624 [25] E. Karabelas, M. A. F. Gsell, G. Haase, G. Plank, C. M. Augustin, An  
 625 accurate, robust, and efficient finite element framework with applications to  
 626 anisotropic, nearly and fully incompressible elasticity, Computer Methods  
 627 in Applied Mechanics and Engineering 394 (2022) 114887.
- 628 [26] R. Codina, I. Castañar, J. Baiges, Finite element approximation of stabi-  
 629 lized mixed models in finite strain hyperelasticity involving displacements  
 630 and stresses and/or pressure—An overview of alternatives, International  
 631 Journal for Numerical Methods in Engineering (2024) e7540.
- 632 [27] L. Moreno, R. Wuechner, A. Larese, A mixed stabilized MPM formula-  
 633 tion for incompressible hyperelastic materials using Variational Subgrid-  
 634 Scales, Computer Methods in Applied Mechanics and Engineering 435  
 635 (2025) 117621.
- 636 [28] T. J. R. Hughes, L. P. Franca, M. Balestra, A new finite element formu-  
 637 lation for computational fluid dynamics: V. Circumventing the babuška-  
 638 brezzi condition: A stable Petrov-Galerkin formulation of the stokes prob-  
 639 lem accommodating equal-order interpolations, Computer Methods in Ap-  
 640 plied Mechanics and Engineering 59 (1) (1986) 85–99.
- 641 [29] A. N. Brooks, T. J. R. Hughes, Streamline upwind/Petrov-Galerkin formu-  
 642 lations for convection dominated flows with particular emphasis on the in-  
 643 compressible Navier-Stokes equations, Computer Methods in Applied Me-  
 644 chanics and Engineering 32 (1) (1982) 199–259.
- 645 [30] L. He, L. Jing, M. Feng, New stabilized mixed finite element methods for  
 646 two-field poroelasticity with low permeability, Applied Mathematics and  
 647 Computation 494 (2025) 129285.
- 648 [31] D. N. Arnold, F. Brezzi, M. Fortin, A stable finite element for the Stokes  
 649 equations, CALCOLO 21 (4) (1984) 337–344.
- 650 [32] F. Auricchio, L. Beirão da Veiga, C. Lovadina, A. Reali, A stability study of  
 651 some mixed finite elements for large deformation elasticity problems, Com-  
 652 puter Methods in Applied Mechanics and Engineering 194 (9-11) (2005)  
 653 1075–1092.
- 654 [33] A. Quarteroni, A. Valli, Numerical Approximation of Partial Differen-  
 655 tial Equations, Springer Series in Computational Mathematics, Springer,  
 656 Berlin, 1994.
- 657 [34] M. Crouzeix, P. Raviart, Conforming and nonconforming finite ele-  
 658 ment methods for solving the stationary Stokes equations I, Revue

- 659       française d'automatique informatique recherche opérationnelle. Mathéma-  
 660       tique 7 (R3) (1973) 33–75.
- 661     [35] U. Brink, E. Stein, On some mixed finite element methods for incompress-  
 662       ible and nearly incompressible finite elasticity, Computational Mechanics  
 663       19 (1) (1996) 105–119.
- 664     [36] T. Belytschko, Y. Y. Lu, L. Gu, Element-free Galerkin methods, Interna-  
 665       tional Journal for Numerical Methods in Engineering 37 (2) (1994) 229–256.
- 666     [37] W. K. Liu, S. Jun, Y. F. Zhang, Reproducing kernel particle methods, Interna-  
 667       tional Journal for Numerical Methods in Fluids 20 (8-9) (1995) 1081–  
 668       1106.
- 669     [38] C. Rodriguez, T.-H. Huang, A variationally consistent reproducing ker-  
 670       nel enhanced material point method and its applications to incompressible  
 671       materials, Computational Mechanics (2023) 1–20.
- 672     [39] S. W. Chi, J. S. Chen, H. Y. Hu, A weighted collocation on the strong form  
 673       with mixed radial basis approximations for incompressible linear elasticity,  
 674       Computational Mechanics 53 (2) (2014) 309–324.
- 675     [40] L. Wang, Z. Qian, Y. Zhou, Y. Peng, A weighted meshfree collocation  
 676       method for incompressible flows using radial basis functions, Journal of  
 677       Computational Physics 401 (2020) 108964.
- 678     [41] A. Ortiz-Bernardin, M. Puso, N. Sukumar, Improved robustness for nearly-  
 679       incompressible large deformation meshfree simulations on Delaunay tes-  
 680       sellations, Computer Methods in Applied Mechanics and Engineering 293  
 681       (2015) 348–374.
- 682     [42] T. J. Hughes, J. A. Cottrell, Y. Bazilevs, Isogeometric analysis: CAD,  
 683       finite elements, NURBS, exact geometry and mesh refinement, Computer  
 684       Methods in Applied Mechanics and Engineering 194 (39-41) (2005) 4135–  
 685       4195.
- 686     [43] F. Auricchio, L. Beirão da Veiga, C. Lovadina, A. Reali, The importance  
 687       of the exact satisfaction of the incompressibility constraint in nonlinear  
 688       elasticity: Mixed FEMs versus NURBS-based approximations, Computer  
 689       Methods in Applied Mechanics and Engineering 199 (5) (2010) 314–323.
- 690     [44] A. Huerta, S. Fernández-Méndez, Locking in the incompressible limit for  
 691       the element-free Galerkin method, International Journal for Numerical  
 692       Methods in Engineering 51 (11) (2001) 1361–1383.
- 693     [45] J. Dolbow, T. Belytschko, Volumetric locking in the element free Galerkin  
 694       method, International Journal for Numerical Methods in Engineering 46 (6)  
 695       (1999) 925–942.

- 696 [46] G. Moutsanidis, J. J. Koester, M. R. Tupek, J.-S. Chen, Y. Bazilevs, Treatment  
 697 of near-incompressibility in meshfree and immersed-particle methods,  
 698 *Computational Particle Mechanics* 7 (2) (2020) 309–327.
- 699 [47] G. Moutsanidis, W. Li, Y. Bazilevs, Reduced quadrature for FEM, IGA  
 700 and meshfree methods, *Computer Methods in Applied Mechanics and En-*  
 701 *gineering* 373 (2021) 113521.
- 702 [48] Z.-Y. Wang, Y.-F. Jin, Z.-Y. Yin, Y.-Z. Wang, Overcoming volumetric  
 703 locking in stable node-based smoothed particle finite element method with  
 704 cubic bubble function and selective integration, *International Journal for*  
 705 *Numerical Methods in Engineering* 123 (24) (2022) 6148–6169.
- 706 [49] T. Elguedj, Y. Bazilevs, V. Calo, T. Hughes,  $B^-$  and  $F^-$  projection meth-  
 707 ods for nearly incompressible linear and non-linear elasticity and plasticity  
 708 using higher-order NURBS elements, *Computer Methods in Applied Me-*  
 709 *chanics and Engineering* 197 (33-40) (2008) 2732–2762.
- 710 [50] J. S. Chen, S. Yoon, H. P. Wang, W. K. Liu, An improved reproducing  
 711 kernel particle method for nearly incompressible finite elasticity, *Computer*  
 712 *Methods in Applied Mechanics and Engineering* 181 (1) (2000) 117–145.
- 713 [51] C. M. Goh, P. M. F. Nielsen, M. P. Nash, A stabilised mixed mesh-  
 714 free method for incompressible media: Application to linear elasticity and  
 715 Stokes flow, *Computer Methods in Applied Mechanics and Engineering* 329  
 716 (2018) 575–598.
- 717 [52] D. S. Bombarde, M. Agrawal, S. S. Gautam, A. Nandy, Hellinger–Reissner  
 718 principle based stress–displacement formulation for three-dimensional iso-  
 719 geometric analysis in linear elasticity, *Computer Methods in Applied Me-*  
 720 *chanics and Engineering* 394 (2022) 114920.
- 721 [53] H. Casquero, M. Golestanian, Vanquishing volumetric locking in quadratic  
 722 NURBS-based discretizations of nearly-incompressible linear elasticity:  
 723 CAS elements, *Computational Mechanics* 73 (6) (2024) 1241–1252.
- 724 [54] A. Huerta, Y. Vidal, P. Villon, Pseudo-divergence-free element free  
 725 Galerkin method for incompressible fluid flow, *Computer Methods in Ap-*  
 726 *plied Mechanics and Engineering* 193 (12-14) (2004) 1119–1136.
- 727 [55] C. T. Wu, W. Hu, J. S. Chen, A meshfree-enriched finite element method  
 728 for compressible and near-incompressible elasticity, *International Journal*  
 729 *for Numerical Methods in Engineering* 90 (7) (2012) 882–914.
- 730 [56] T. Vu-Huu, C. Le-Thanh, H. Nguyen-Xuan, M. Abdel-Wahab, A high-  
 731 order mixed polygonal finite element for incompressible Stokes flow analy-  
 732 sis, *Computer Methods in Applied Mechanics and Engineering* 356 (2019)  
 733 175–198.

- 734 [57] E. Stein, R. de Borst, T. J. R. Hughes (Eds.), Encyclopedia of Computational Mechanics, John Wiley, Chichester, West Sussex, 2004.
- 735
- 736 [58] I. Babuška, J. Osborn, Eigenvalue Problems, in: Handbook of Numerical Analysis, Vol. 2 of Finite Element Methods (Part 1), Elsevier, 1991, pp. 641–787.
- 737
- 738
- 739 [59] K. Yosida, Functional Analysis, 6th Edition, Classics in Mathematics, Springer-Verlag, Berlin Heidelberg, 1995.
- 740
- 741 [60] J. Wu, D. Wang, An accuracy analysis of Galerkin meshfree methods accounting for numerical integration, Computer Methods in Applied Mechanics and Engineering 375 (2021) 113631.
- 742
- 743
- 744 [61] S. Timoshenko, J. Goodier, Theory of Elasticity, Engineering Mechanics Series, McGraw-Hill, 1969.
- 745
- 746 [62] S. Reese, P. Wriggers, B. D. Reddy, A new locking-free brick element technique for large deformation problems in elasticity, Computers & Structures 75 (3) (2000) 291–304.
- 747
- 748
- 749 [63] S. C. Brenner, L. R. Scott, The Mathematical Theory of Finite Element Methods, Springer, New York, 2008.
- 750

751    **Appendix A. Error estimator for mixed-formulation**

752    In this appendix, the traditional error estimators for mixed-formulation are  
 753    illustrated herein, the proof is referred to [63]. For incompressible elasticity  
 754    problems, i.e.  $\kappa \rightarrow \infty$ ,  $c(q, p) = 0$ , the weak formula of Eq. (14) is rewritten as:  
 755    Find  $\mathbf{u}_h \in V_h, p_h \in Q_h$ ,

$$\begin{aligned} a(\mathbf{v}_h, \mathbf{u}_h) + b(\mathbf{v}_h, p_h) &= f(\mathbf{v}_h), & \forall \mathbf{v}_h \in V_h \\ b(\mathbf{u}_h, q_h) &= 0, & \forall q_h \in Q_h \end{aligned} \quad (\text{A.1})$$

756    According to the definition of bilinear form  $b$  in Eq. (10), for a  $\mathbf{u}_h \in \ker \mathcal{P}_h$ , then  
 757    the second equation of Eq. (A.1) is naturally satisfied. Thus, the above weak  
 758    formulation can be equivalently split into the following two steps: Firstly, find  
 759     $\mathbf{u}_h \in \ker \mathcal{P}_h$ ,

$$a(\mathbf{v}_h, \mathbf{u}_h) = f(\mathbf{v}_h), \quad \forall \mathbf{v}_h \in \ker \mathcal{P}_h \quad (\text{A.2})$$

760    After determine  $\mathbf{u}_h$ , then find  $p_h \in Q_h$ ,

$$b(\mathbf{v}_h, p_h) = f(\mathbf{v}_h) - a(\mathbf{v}_h, \mathbf{u}_h), \quad \forall \mathbf{v}_h \in V_h \quad (\text{A.3})$$

761    To further analyze the error of mixed-formulation, the following properties  
 762    of bilinear forms  $a$  and  $b$  should be defined [63]:

763    • **Continuity:**

$$a(\mathbf{v}, \mathbf{u}) \leq C_a \|\mathbf{v}\|_V \|\mathbf{u}\|_V, \quad \forall \mathbf{v}, \mathbf{u} \in V \quad (\text{A.4})$$

$$b(\mathbf{v}, q) \leq C_b \|\mathbf{v}\|_V \|q\|_Q, \quad \forall \mathbf{v} \in V, \forall q \in Q \quad (\text{A.5})$$

764    • **Coercivity:**

$$\|\mathbf{v}\|_V \leq \frac{1}{\alpha} \sup_{\mathbf{w} \in V} \frac{|a(\mathbf{v}, \mathbf{w})|}{\|\mathbf{w}\|_V}, \quad \forall \mathbf{v} \in V \quad (\text{A.6})$$

765    • **Inf-sup condition:**

$$\|q\|_Q \leq \frac{1}{\beta} \sup_{\mathbf{v} \in V} \frac{|b(\mathbf{v}, q)|}{\|\mathbf{v}\|_V}, \quad \forall q \in Q \quad (\text{A.7})$$

766    where  $C_a$  and  $C_b$  are positive constants independent of mesh size  $h$ .  $\alpha$  and  $\beta$   
 767    are the coercivity and inf-sup constants, respectively, which will influence the  
 768    accuracy of mixed-formulation.

769    For the error of displacement, the Céa's Theorem used for the error analysis  
 770    of traditional Galerkin formulation is not always valid for mixed-formulation.  
 771    This is because most of mixed-formulation can not ensure  $\ker \mathcal{P}_h \subset \ker \mathcal{P}$  to  
 772    maintain the orthogonality of bilinear form  $a$  that is required in the proof of  
 773    Céa's Theorem. So we first introduce the following error estimator for displacement  
 774    in the case of  $\ker \mathcal{P}_h \not\subset \ker \mathcal{P}$ . For any  $\mathbf{v}_h \in \ker \mathcal{P}_h$ , considering the triangle

775 inequality, the coercivity in Eq. (A.6) and the continuity in Eq. (A.4), we have:

$$\begin{aligned}
\|\mathbf{u} - \mathbf{u}_h\|_V &\leq \|\mathbf{u} - \mathbf{v}_h\|_V + \|\mathbf{v}_h - \mathbf{u}_h\|_V \\
&\leq \|\mathbf{u} - \mathbf{v}_h\|_V + \frac{1}{\alpha} \sup_{\mathbf{w}_h \in \ker \mathcal{P}_h} \frac{|a(\mathbf{v}_h - \mathbf{u}_h, \mathbf{w}_h)|}{\|\mathbf{w}_h\|_V} \\
&\leq \|\mathbf{u} - \mathbf{v}_h\|_V + \frac{1}{\alpha} \sup_{\mathbf{w}_h \in \ker \mathcal{P}_h} \frac{|a(\mathbf{v}_h - \mathbf{u}, \mathbf{w}_h)| + |a(\mathbf{u} - \mathbf{u}_h, \mathbf{w}_h)|}{\|\mathbf{w}_h\|_V} \\
&\leq (1 + \frac{C}{\alpha}) \|\mathbf{u} - \mathbf{v}_h\|_V + \frac{1}{\alpha} \sup_{\mathbf{w}_h \in \ker \mathcal{P}_h} \frac{|a(\mathbf{u} - \mathbf{u}_h, \mathbf{w}_h)|}{\|\mathbf{w}_h\|_V}
\end{aligned} \tag{A.8}$$

776 According to Eqs. (A.2), (A.3) and continuity in Eq. (A.5), the second term on  
777 the right hand side of above equation can be rewritten as:

$$\begin{aligned}
\sup_{\mathbf{w}_h \in \ker \mathcal{P}_h} \frac{|a(\mathbf{u} - \mathbf{u}_h, \mathbf{w}_h)|}{\|\mathbf{w}_h\|_V} &= \sup_{\mathbf{w}_h \in \ker \mathcal{P}_h} \frac{|a(\mathbf{u}, \mathbf{w}_h) - f(\mathbf{w}_h)|}{\|\mathbf{w}_h\|_V} \\
&= \sup_{\mathbf{w}_h \in \ker \mathcal{P}_h} \frac{|b(\mathbf{w}_h, p)|}{\|\mathbf{w}_h\|_V} \\
&= \sup_{\mathbf{w}_h \in \ker \mathcal{P}_h} \frac{|b(\mathbf{w}_h, p - q_h)|}{\|\mathbf{w}_h\|_V} \\
&\leq C_b \|p - q_h\|_Q
\end{aligned} \tag{A.9}$$

778 where  $q_h$  is an arbitrary variable in  $Q_h$ . Combining the Eqs. (A.8) and (A.9),  
779 the following error estimator for displacement can be obtained:

$$\|\mathbf{u} - \mathbf{u}_h\|_V \leq (1 + \frac{C_a}{\alpha}) \inf_{\mathbf{v}_h \in \ker \mathcal{P}_h} \|\mathbf{u} - \mathbf{v}_h\|_V + \frac{C_b}{\alpha} \inf_{q_h \in Q_h} \|p - q_h\|_Q \tag{A.10}$$

780 Furthermore, for the error estimator of pressure, according to the first equa-  
781 tion of Eq. (6) and  $V_h \subset V$ , we have:

$$b(\mathbf{v}_h, p) = f(\mathbf{v}_h) - a(\mathbf{v}_h, \mathbf{u}), \quad \forall \mathbf{v}_h \in V_h \tag{A.11}$$

782 and then subtracting Eq. (A.11) from Eq. (A.3) yields:

$$b(\mathbf{v}_h, p - p_h) = -a(\mathbf{v}_h, \mathbf{u} - \mathbf{u}_h), \quad \forall \mathbf{v}_h \in V_h \tag{A.12}$$

783 In this context, for any  $q_h \in Q_h$ , invoking the triangle inequality, Eqs. (A.7)  
784 and (A.5) leads to:

$$\begin{aligned}
\|p - p_h\|_Q &\leq \|p - q_h\|_Q + \|q_h - p_h\|_Q \\
&\leq \|p - q_h\|_Q + \frac{1}{\beta} \sup_{\mathbf{v} \in V_h} \frac{|b(\mathbf{v}_h, q_h - p_h)|}{\|\mathbf{v}_h\|_V} \\
&\leq \|p - q_h\|_Q + \frac{1}{\beta} \sup_{\mathbf{v} \in V_h} \frac{|a(\mathbf{v}_h, \mathbf{u} - \mathbf{u}_h)| + |b(\mathbf{v}_h, p - q_h)|}{\|\mathbf{v}_h\|_V} \\
&\leq \frac{C_a}{\beta} \|\mathbf{u} - \mathbf{u}_h\|_V + (1 + \frac{C_b}{\beta}) \|p - q_h\|_Q
\end{aligned} \tag{A.13}$$

785 Consequently, the error estimator for pressure can be given by:

$$\|p - p_h\|_Q \leq \frac{C_a}{\beta} \|\mathbf{u} - \mathbf{u}_h\|_V + \left(1 + \frac{C_b}{\beta}\right) \inf_{q_h \in Q_h} \|p - q_h\|_Q \quad (\text{A.14})$$

786 Obviously, the error estimators of Eqs. (A.10) and (A.14) are both related  
 787 to the coercivity constant  $\alpha$ , inf-sup constant  $\beta$  and the approximability of  
 788 spaces  $\ker \mathcal{P}_h$ ,  $Q_h$ , in which the approximability is usually measured by the  
 789 interpolation error of approximation method. However, the approximability  
 790 of space  $\ker \mathcal{P}_h$  is not trivial to be evaluated directly. To further evaluate the  
 791 approximability of space  $\ker \mathcal{P}_h$ , let a variable  $\mathbf{w}_h \in V_h \setminus \ker \mathcal{P}_h$  to satisfy the  
 792 following relationship:

$$\inf_{\bar{\mathbf{v}}_h \in \ker \mathcal{P}_h} \|\mathbf{u} - (\bar{\mathbf{v}}_h + \mathbf{w}_h)\|_V = \inf_{\mathbf{v}_h \in V_h} \|\mathbf{u} - \mathbf{v}_h\|_V \quad (\text{A.15})$$

793 such that the approximability of space  $\ker \mathcal{P}_h$  can be transformed to that of  
 794 space  $V_h$  that is easy to be measured. If  $\mathbf{w}_h = \mathbf{0}$ ,  $\ker \mathcal{P}_h$  has the identical  
 795 approximability with  $V_h$ :

$$\inf_{\bar{\mathbf{v}}_h \in \ker \mathcal{P}_h} \|\mathbf{u} - \bar{\mathbf{v}}_h\|_V = \inf_{\mathbf{v}_h \in V_h} \|\mathbf{u} - \mathbf{v}_h\|_V \quad (\text{A.16})$$

796 If  $\mathbf{w}_h \neq \mathbf{0}$ , leading a triangle inequality we have:

$$\|\mathbf{u} - \bar{\mathbf{v}}_h\|_V \leq \|\mathbf{u} - (\bar{\mathbf{v}}_h + \mathbf{w}_h)\|_V + \|\mathbf{w}_h\|_V \quad (\text{A.17})$$

797 where, reconsidering the Eq. (26) in Lemma 1, as  $\mathbf{w}_h \in V_h \setminus \ker \mathcal{P}_h$  and  $\mathbf{w}_h \neq \mathbf{0}$ ,  
 798 the following relation can be obtained:

$$\|\mathbf{w}_h\|_V \leq \frac{1}{\beta} \|\mathcal{P}_h \mathbf{w}_h\|_Q \quad (\text{A.18})$$

799 where, using Eqs. (25), (17) and considering  $\mathbf{u} \in \ker \mathcal{P}$ ,  $\bar{\mathbf{v}}_h \in \ker \mathcal{P}_h$ , the right  
 800 hand side of above equation can further be transformed as follows:

$$\begin{aligned} \|\mathcal{P}_h \mathbf{w}_h\|_Q &= \sup_{q_h \in Q_h} \frac{|\frac{1}{\kappa}(\mathcal{P}_h \mathbf{w}_h, q_h)|}{\|q_h\|_Q} = \sup_{q_h \in Q_h} \frac{|b(\mathbf{w}_h, q_h)|}{\|q_h\|_Q} \\ &= \sup_{q_h \in Q_h} \frac{|b(\mathbf{u} - (\mathbf{w}_h + \bar{\mathbf{v}}_h), q_h)|}{\|q_h\|_Q} \\ &\leq C_b \|\mathbf{u} - (\mathbf{w}_h + \bar{\mathbf{v}}_h)\|_V \end{aligned} \quad (\text{A.19})$$

801 With the combination of Eqs. (A.17), (A.18) and (A.19), the approximability  
 802 of  $\ker \mathcal{P}_h$  for the case of  $\mathbf{w}_h \neq \mathbf{0}$  is given by:

$$\inf_{\bar{\mathbf{v}}_h \in \ker \mathcal{P}_h} \|\mathbf{u} - \bar{\mathbf{v}}_h\|_V \leq \left(1 + \frac{C_b}{\beta}\right) \inf_{\mathbf{v}_h \in V_h} \|\mathbf{u} - \mathbf{v}_h\|_V \quad (\text{A.20})$$